International Journal of Heat and Fluid Flow 30 (2009) 286–305

Contents lists available at ScienceDirect

International Journal of Heat and Fluid Flow

journal homepage: www.elsevier.com/locate/ijhff

Detached eddy simulation of flow around two wall-mounted cubes in tandem

Joongcheol Paik [a], Fotis Sotiropoulos [b,*], Fernando Porté-Agel [b]

[a] Department of Civil Engineering, Kangnung National University, Gangneung, Gangwon 210-702, South Korea
[b] St. Anthony Falls Laboratory, Department of Civil Engineering, University of Minnesota, Minneapolis, MN 55414, USA

ARTICLE INFO

Article history:
Received 28 July 2007
Received in revised form 28 October 2008
Accepted 17 January 2009
Available online 24 February 2009

Keywords:
Coherent structures
Wall-mounted cubes
Turbulence modeling
DES
URANS

ABSTRACT

We investigate the performance of unsteady Reynolds-averaged Navier–Stokes (URANS) computation and various versions of detached eddy simulation (DES) in resolving coherent structures in turbulent flow around two cubes mounted in tandem on a flat plate at Reynolds number (*Re*) of 22,000 and for a thin incoming boundary layer. Calculations are carried out using four different coherent structure resolving turbulence models: (1) URANS with the Spalart–Allmaras model; (2) the standard DES [Spalart, P.R., Jou, W.H., Strelets, M., Allmaras, S.R., 1997. Comments on the feasibility of LES for wings, and on a hybrid RANS/LES approach. In: Liu, C., Liu, Z., (Eds.), Advances in DNS/LES. Greyden Press, Columbus, OH]; (3) the Delayed DES (DDES); and (4) the DES with a low-*Re* modification (DES-LR) [Spalart, P., Deck, S., Shur, M., Squires, K., Strelets, M., Travin, A., 2006. A new version of detached eddy simulation, resistant to ambiguous grid densities. Theor. Comput. Fluid Dyn. 20 (3), 181–195]. The grid sensitivity of the computed solutions is examined by carrying out simulations on two successively refined grids. The computed results for all cases are compared with the experimental measurements of Martinuzzi and Havel [Martinuzzi, R., Havel, B., 2000. Turbulent flow around two interfering surface-mounted cubic obstacles in tandem arrangement. ASME J. Fluids Eng. 122, 24–31] for two different cube spacings. All turbulence models reproduce essentially identical separation of the approach thin boundary layer and yield an unsteady horseshoe vortex system consisting of multiple vortices in the leading edge region of the upstream cube. Significant discrepancies between the URANS and all DES solutions are observed, however, in other regions of interest such as the shear layers emanating from the cubes, the inter-cube gap and the downstream wake. Regardless of the grid refinement, URANS fails to capture key features of the mean flow, including the second horseshoe vortex in the upstream junction and recirculating flow on the top surface of the downstream cube for the large cube spacing, and underestimates significantly turbulence statistics in most regions of the flow for both cases. On the coarse mesh, all three DES approaches appear to yield very similar results and fail to reproduce the second horseshoe vortex. The standard DES and DDES solutions obtained on the fine meshes are essentially identical and both suffer from premature switching to unresolved DNS, due to the mis-interpretation of grid refinement as wall proximity, which leads to spurious vortices in the inter-cube region. Numerical solutions show that the low-*Re* modification (DES-LR) is critical prerequisite in DES on the ambiguously fine – not fine enough for full LES – mesh to prevent excessive nonlinear drop of the subgrid eddy viscosity in low cell-*Re* regions like in the inter-obstacle gap. Mean flow quantities and turbulence statistics obtained with DES-LR on the fine mesh are in good overall agreement with the measurements in most regions of interest for both cases.

1. Introduction

Turbulent flows around surface-mounted three-dimensional obstacles are characterized by complex flow phenomena such as, among others, three-dimensional separation and horseshoe vortex formation in the junction region, quasi-periodic vortex shedding in the shear layer emanating from sharp obstacle edges, low-frequency bimodal oscillations of velocity fields, multiple recirculation zones and wake structures (Devenport and Simpson, 1990; Hussein and Martinuzzi, 1996; Yakhot et al., 2006; Paik et al., 2007). These phenomena lead to the formation of dynamically rich coherent vortical structures which interact with each other and the surrounding solid surfaces and play an important roll in particle transport and heat transfer in many aerodynamics and hydrodynamics applications.

Turbulent flow around a single wall-mounted cube has long been used as benchmark case and studied extensively experimentally to understand the basic flow topology and rich dynamics of coherent vortical structures around surface-mounted obstacles (e.g. Castro and Robins, 1977; Schofield and Logan, 1990; Martinuzzi and Tropea, 1993; Hussein and Martinuzzi, 1996). Among

---

* Corresponding author. Tel.: +1 612 624 2022.
E-mail address: fotis@umn.edu (F. Sotiropoulos).

0142-727X/$ - see front matter © 2009 Elsevier Inc. All rights reserved.
doi:10.1016/j.ijheatfluidflow.2009.01.006

the various experiments reported in the literature, Martinuzzi and Tropea (1993) reported one of the most detailed experimental measurements and flow visualizations at Reynolds number (*Re*) of 40,000 based on the cube height. Experimental investigations of more complex cases involving flows past multiple surface-mounted obstacles, on the other hand, are rather scarce. Meinders and Hanjalić (1999) conducted experimental measurements of flow over an array of wall-mounted cubes at a low-*Re* ($Re = 3854$ based on the cube height). More recently, experimental investigations of flows past two wall-mounted cubes have been carried out at moderate ($Re = 22{,}000$) (Martinuzzi and Havel, 2000) and low ($Re = 3{,}900$) (Meinders and Hanjalić, 2002) Reynolds numbers.

A number of numerical predictions of the flow around a single cube at $Re = 40{,}000$ (Martinuzzi and Tropea, 1993) have been reported in the literature using Reynolds-averaged Navier–Stokes (RANS), unsteady RANS (URANS) and large-eddy simulation (LES) turbulence models (Rodi, 1997; Rodi et al., 1997; Shah and Ferziger, 1997; Krajnović and Davidson, 2002; Iaccarino et al., 2003). Three main conclusions can be drawn from these studies: (1) steady RANS simulations yield poor predictions of most aspects of such flows, including the prediction of essential features of the mean flow (Rodi, 1997; Iaccarino et al., 2003); (2) URANS with careful treatment of the near-wall region yields acceptable mean flow fields but fails to reproduce turbulence statistics induced by rich dynamics of coherent structures around and in the wake of the obstacle (Rodi, 1997; Iaccarino et al., 2003); (3) LES with appropriate (turbulent) inflow boundary conditions yields mean flow and turbulence statistics that are in reasonably good agreement with the measurements (Shah and Ferziger, 1997; Rodi, 1997; Rodi et al., 1997; Krajnović and Davidson, 2002). Flows past an array of cubes have also been studied numerically (Meinders and Hanjalić, 1999) using URANS, detached eddy simulation (DES) (Schmidt and Thiele, 2002), and LES (Ničeno et al., 2002). All these studies assumed spatial periodicity in both streamwise and spanwise directions and showed that DES and other hybrid URANS/LES approaches are promising engineering tools for practical simulations of such flows.

Numerical simulations of flows past two surface-mounted cubes, where the assumption of flow periodicity is no longer valid, have yet to be reported in the literature. In the experiments of Martinuzzi and Havel (2000), which studied the flow past two cubes in tandem, it was observed that for Reynolds numbers in the range $3000 < Re < 40{,}000$ the flow around the cubes is only weakly sensitive to Reynolds number. In particular, their detailed measurements at $Re = 22{,}000$ are considered to be representative for all Reynolds numbers in the range $12{,}000 < Re < 40{,}000$. Through a series of experiments for a wide range of cube spacings, they observed that depending on the distance between the cubes three distinct flow patterns exist. For small spacings, the shear layer separating from the first cube reattaches on the sides of the second obstacle and periodic vortex shedding can only be detected in the wake of the downstream cube – i.e. the two cubes essentially act as a single bluff body. Above a critical spacing range, Martinuzzi and Havel (2000) observed fluctuations in the inter-cube gap and wake lock-in phenomena for three-dimensional tandem geometries, and discussed details of the distinct features of the mean velocity field in the lock-in regime and the shedding mechanism of the wake at different phases of the shedding cycle (also, see Martinuzzi and Havel, 2000 for details). For larger spacings, a second horseshoe vortex appears at the windward base of the second cube (Martinuzzi and Havel, 2000).

In this study, we report the first (to the best of our knowledge) numerical simulations for the experiments of Martinuzzi and Havel (2000) for two different cube spacings corresponding to 2 and 4 times the cube height, respectively. The objective of these simulations is twofold: (1) to carry out a comprehensive assessment of the predictive capabilities of various coherent structure resolving turbulence models based on URANS and DES; and (2) to contribute to the understanding of the rich coherent dynamics of such flows. We carry out calculations using URANS with the Spalart–Allmaras (S–A) model, the original DES approach (Spalart et al., 1997) and two recently proposed variants of DES, the so-called delayed DES (DDES) and DES with low-Reynolds number correction (DES-LR) (Spalart et al., 2006).

DES was originally proposed by Spalart et al., 1997. It is a hybrid URANS/LES approach based on the one-equation S–A eddy viscosity model and has been successfully applied to resolve rich dynamics of coherent structures over complex geometrical configurations at practical Reynolds numbers using affordable computational resources (Hedges et al., 2002; Paik and Sotiropoulos, 2005; Krishnan et al., 2006a). In spite of the promise of this approach, however, two critical deficiencies of the standard model have been identified and already discussed extensively in the literature. First, in the standard DES the boundary layers are treated entirely with the URANS model by generating a grid with large grid spacing parallel to the wall as is common practice in conventional wall-resolving RANS calculations. In practical application, however, the grid spacing parallel to the wall may become less than the boundary layer thickness δ – e.g. through the boundary layer thickening or grid refinement in the junction region confined by two walls. From the DES standpoint, such grid structure implies that the LES mode of the model will be activated prematurely in the attached region of the flow where coherent unsteadiness has not yet emerged in the computed solutions. Consequently, the instantaneous flow fields do not have a sufficient level of Reynolds stresses to support a turbulent-like LES computation, and the flow separates spuriously in a laminar-like fashion. This strong dependence of the DES and similar hybrid URANS/LES approaches on the grid structure has been recognized by Spalart et al. (1997) and also discussed and demonstrated by others in recent studies (Menter et al., 2003; Paik et al., 2007). Spalart et al. (2006) eloquently referred to this deficiency of DES as *modeled-stress depletion*. The second deficiency of DES stems from the fact that for the S–A subgrid model used in the LES mode of the standard approach the subgrid eddy viscosity decreases with both decreasing grid spacing and local flow Reynolds number. Therefore, the standard model misinterprets a local grid refinement below a threshold level as *wall proximity*, which results in excessive non-linear drop of subgrid viscosity relative to the ambient velocity and length scales (Spalart et al., 2006). This fast nonlinear drop of ν_t gives rise to a premature switch to “no-model” computation (i.e. unresolved DNS) in regions of the flow where the local Reynolds number is sufficiently low. Such situation could typically occur in the downstream region of surface-mounted obstacles where flow separation in the wake in conjunction with the presence of solid surfaces could result in very low flow velocities. To eliminate these two potentially very serious in practical applications deficiencies, Spalart et al. (2006) recently proposed the two modified versions of DES which are evaluated in this work: (1) DDES to remedy modeled-stress depletion; and (2) DES-LR to address the issue of premature switch to unresolved DNS.

The flow past two wall-mounted cubes is an excellent test case for evaluating the performance of the various DES versions. The geometrical complexity of the computational domain coupled with the multi-faceted physics of the flow requires for accurate discretization of the flow domain the use of computational meshes that bring out both of the aforementioned deficiencies of the standard DES model. For both cube spacings considered herein, for instance, the computational domain is discretized using domain decomposition with a total of 12 overset chimera grids. The grid sensitivity of the computed solutions is examined by carrying out simulations on two meshes: a coarse mesh with approximately 0.82×10^6;

and a fine mesh with approximately 2.1×10^6 grid nodes, which is obtained by refining the coarse mesh by a factor of 3/2 in all three spatial directions. The grid spacing on the fine mesh is such that the LES mode of DES is activated in all regions of interest in the flow, but is patently not fine enough to fully support LES content. The resulting ambiguously fine grid structure will cause the standard DES to suffer both from modeled-stress depletion and premature switch to under-resolved DNS in regions of low local Reynolds number, thus, allowing us to evaluate the effectiveness of the two recent remedies reported in Spalart et al. (2006).

The paper is organized as follows. First we present the governing equations and a brief description of the numerical approach and computational details. Next, along with our grid refinement study, we discuss the features of the time-averaged flow along with comparison with the experimental measurements (Martinuzzi and Havel, 2000; Martinuzzi and Havel, 2004). It is followed by the presentation of two- and three-dimensional coherent vortical structures resolved on our fine grid and identified by visualization techniques, and the comparison of computed turbulent statistics with the measurements. Finally, conclusions are drawn.

2. Numerical methodology

2.1. Governing equations

The governing equations for the mean flow are the three-dimensional, unsteady, incompressible, RANS equations. The equations are formulated in generalized curvilinear coordinates and read in strong-conservation form as follows:

$$\Gamma \frac{\partial Q}{\partial t} + J \frac{\partial}{\partial \xi^j}(F^j - F^j_v) = 0 \tag{1}$$

where

$$\begin{aligned}
&\Gamma = \mathrm{diag}[0, 1, 1, 1] \\
&Q = [P, u_1, u_2, u_3]^T \\
&F^j = \frac{1}{J}\left[U^j, u_1 U^j + P\xi^j_{x_1}, u_2 U^j + P\xi^j_{x_2}, u_3 U^j + P\xi^j_{x_3}\right]^T \\
&F^j_v = \frac{1}{J}\left(\frac{1}{Re} + \nu_t\right)\left[0, g^{mj}\frac{\partial u_1}{\partial \xi^m} + R_{m1}\xi^j_{x_m}, g^{mj}\frac{\partial u_2}{\partial \xi^m}\right. \\
&\qquad \left. + R_{m2}\xi^j_{x_m}, g^{mj}\frac{\partial u_3}{\partial \xi^m} + R_{m3}\xi^j_{x_m}\right]^T
\end{aligned}$$

In the equations above, the term P is a modified pressure $P = p/\rho + 2k/3$ where p is the piezometric pressure and k is the turbulence kinetic energy, $u_i (i = 1, 2, 3)$ are the resolved Cartesian velocity components, x_i are the Cartesian coordinates, J is the Jacobian of the geometric transformation, $\xi^j_{x_i}$ are the metrics of the geometric transformation, U^j are the contravariant velocity components $U^j = u_i \xi^j_{x_i}$, g^{ij} are the components of the contravariant metric tensor $g^{ij} = \xi^i_{x_k}\xi^j_{x_k}$, Re is the Reynolds number, ν_t is the turbulent viscosity which is introduced by adopting the Boussinesq's assumption for modeling the unresolved stresses, and R_{ij} is the velocity gradient tensor $R_{ij} = (\partial u_j / \partial \xi^k)\xi^i_{x_j}$.

2.2. Turbulence models

The DES technique, proposed by Spalart et al. (1997), is based on the S–A eddy viscosity model (Spalart and Allmaras, 1994), which solves a single transport equation for a working variable $\tilde{\nu}$ that is related to the turbulent viscosity ν_t. This model includes a wall destruction term, which reduces the turbulent viscosity in the logarithmic layer and laminar sublayer, as well as transition terms, which provide a smooth transition from laminar to turbulent flow (Spalart and Allmaras, 1994). After neglecting the transition terms, which are not necessary in the present simulations, the transport equation reads as follows:

$$\frac{1}{J}\frac{\partial \tilde{\nu}}{\partial t} + \frac{\partial}{\partial \xi^j}[F^j_t - F^j_{t\nu}] + H_t = 0 \tag{2}$$

where

$$\begin{aligned}
&F^j_t = \frac{1}{J}[U^j \tilde{\nu}] \\
&F^j_{t\nu} = \frac{1}{J}\left[\frac{1}{\sigma}\left(\frac{1}{Re} + \tilde{\nu}\right) g^{mj}\frac{\partial \tilde{\nu}}{\partial \xi^m}\right] \\
&H_t = \frac{1}{J}\left[-c_{b1}(1 - f_{t2})\tilde{S}\tilde{\nu} + \left(c_{w1}f_w - \frac{c_{b1}}{\kappa^2}f_{t2}\right)\left(\frac{\tilde{\nu}}{d}\right)^2 - \frac{1}{\sigma}c_{b2}g^{mj}\frac{\partial \tilde{\nu}}{\partial \xi^m}\frac{\partial \tilde{\nu}}{\partial \xi^m}\right]
\end{aligned}$$

The turbulent viscosity ν_t is linked to the working variable $\tilde{\nu}$ and a wall function f_{v1} by

$$\nu_t = \tilde{\nu} f_{v1}, \quad f_{v1} = \frac{\chi^3}{\chi^3 + c^3_{v1}}, \quad \chi = \frac{\tilde{\nu}}{\nu} \tag{3}$$

where ν is the molecular viscosity. The modified vorticity $\tilde{S}$ is defined in terms of the magnitude of the vorticity S as,

$$\begin{aligned}
&\tilde{S} \equiv f_{v3}S + \frac{\tilde{\nu}}{\kappa^2 \tilde{d}^2} f_{v2}, \quad f_{v2} = \left(1 + \frac{\chi}{c_{v2}}\right)^{-3}, \\
&f_{v3} = \frac{(1 + \chi f_{v1})(1 - f_{v2})}{\chi}
\end{aligned} \tag{4}$$

where $\tilde{d}$ is the DES length scale (see below). The production term as written in Eq. (4) differs from that developed by Spalart and Allmaras (1994) via the introduction of f_{v3} and re-definition of f_{v2}. These changes do not alter predictions of fully turbulent flows and have the advantage that in simulation of flows with laminar separation, spurious upstream propagation of the eddy viscosity into attached, laminar regions is prevented (Squires et al., 2005). The wall destruction function f_w is given as follows:

$$f_w = g\left[\frac{1 + c^6_{w3}}{g^6 + c^6_{w3}}\right]^{1/6}, \quad g = r + c_{w2}(r^6 - r), \quad r \equiv \frac{\tilde{\nu}}{\tilde{S}\kappa^2\tilde{d}^2} \tag{5}$$

The function f_{t2} is defined as,

$$f_{t2} = c_{t3}\exp(-c_{t4}\chi^2) \tag{6}$$

The closure coefficients are $c_{b1} = 0.1355$, $\sigma = 2/3$, $c_{b2} = 0.622$, $\kappa = 0.41$, $c_{w1} = c_{b1}/\kappa^2 + (1 + c_{b2})/\sigma$, $c_{w2} = 0.3$, $c_{w3} = 2$, $c_{v1} = 7.1$, $c_{v2} = 5$, $c_{t3} = 1.1$ and $c_{t4} = 2$.

In this study, we apply the standard and two modified versions of DES along with URANS based on the numerical solution of the governing equations with the S–A turbulence model in unsteady mode.

2.2.1. DES

DES stands for the standard DES proposed by Spalart et al. (1997). The DES length scale in the S–A model equations depends on the distance from the nearest wall d and the local grid spacing Δ as follows:

$$\tilde{d} \equiv \min(d, C_{\mathrm{DES}}\Delta) \tag{7}$$

where $\Delta \equiv \max(\Delta x, \Delta y, \Delta z)$ is the largest dimension of the grid cell and the additional model constant is set equal to its standard value $C_{\mathrm{DES}} = 0.65$. Assuming that the computational mesh is constructed such that the wall-parallel grid spacing is of the order of the boundary layer thickness, the above length scale definition ensures that the S–A URANS model is retained throughout the boundary layer, i.e., $\tilde{d} = d$. Consequently, prediction of boundary layer separation is determined in the URANS mode of DES. Sufficiently far from solid boundaries $\tilde{d} \sim \Delta$ and the model becomes a one-equation LES model for the sub-grid scale (SGS) eddy viscosity. When the production and destruction terms of the model are balanced, the length scale $\tilde{d} = C_{\mathrm{DES}}\Delta$ in the LES region yields a Smagorinsky eddy viscosity $\tilde{\nu} \propto S\Delta^2$. Analogous to classical LES, the role of Δ is to allow the energy cascade down from the resolved to the sub-grid scales; roughly, it makes the pseudo-Kolmogorov length scale, based on the eddy viscosity, proportional to the grid spacing.

2.2.2. DDES

DDES denotes the delayed DES model, which is proposed by Spalart et al. (2006) to preserve the RANS mode (or to delay the LES mode) in the boundary layer, even if Δ is much less than δ. The modification of the standard model of Spalart et al. (1997) is analogous to that in Menter et al. (2003) which uses the blending functions of the SST model. DDES redefines the length scale $\tilde{d}$ to preserve the URANS treatment of the boundary layer via the model function f_d as follows:

$$\tilde{d} \equiv d - f_d \max(0, d - C_{\mathrm{DES}}\Delta) \tag{8}$$

The function f_d is defined as,

$$f_d \equiv 1 - \tanh([8r_d]^3) \tag{9}$$

The quantity r_d used in the function f_d is a modified expression of r in the S–A model given as,

$$r_d \equiv \frac{\nu_t + \nu}{\sqrt{u_{i,j}u_{i,j}}\kappa^2 d^2} \tag{10}$$

where $u_{i,j}$ are the velocity gradients. Similar to r in the S–A model, r_d equals 1 in a logarithmic layer, and falls to 0 gradually toward the edge of the boundary. Subsequently, the function f_d is designed to be 1 in the LES region, where $r_d \ll 1$, and 0 elsewhere (near-wall region). The constants 8 and 3 are based on shape requirements for f_d and on tests of DDES in the flat plate boundary layer, which ensure that the solution inside the entire boundary layer is essentially identical to the RANS solution, regardless of the grid spacing (see Spalart et al., 2006 for details).

2.2.3. DES-LR

DES-LR denotes the DES with a low-Reynolds number correction proposed by Spalart et al. (2006) against the premature switch of the standard DES to unresolved DNS in low cell-*Re* regions. In the DES-LR, the length scale $\tilde{d}$ is redefined via introducing the model function $\Psi \geqslant 1$ which is a function of ν_t/ν, or equivalently of the parameter χ in the S–A model:

$$\tilde{d} \equiv \min(d, \Psi C_{\mathrm{DES}}\Delta) \tag{11}$$

where

$$\Psi^2 = \min\left[10^2, \frac{1 - \frac{c_{b1}}{c_{w1}\kappa^2 f_w^*}[f_{t2} + (1 - f_{t2})f_{v2}]}{f_{v1}\max(10^{-10}, 1 - f_{t2})}\right] \tag{12}$$

The quantity f_w^*(=0.424) is the limit value of the equilibrium function f_w at high subgrid viscosity. The derivation of the expression is based on the assumption that at equilibrium the modified subgrid model driven by $\tilde{d} = \Psi C_{\mathrm{DES}}\Delta$ should reduce to a Smagorinsky-like model, i.e., $\nu_t = (C\Delta)^2 S$ where C is constant. The function Ψ and $1 - f_{t2}$ are limited to ensure reasonable behavior in the “DNS limit” $\nu_t < \nu/100$. The correction is inactive ($\Psi = 1$) for a subgrid eddy viscosity higher than about 10ν and becomes quite strong for lower values. Note that, instead of the modified versions of f_{v2} and f_{v3} given by Eq. (4), we used the following original functions in the DES-LR model,

$$f_{v2} = 1 - \frac{\chi}{1 + \chi f_{v1}}, \quad f_{v3} = 1 \tag{13}$$

2.3. Numerical method

The governing equations are solved using a dual-time-stepping artificial compressibility (AC) iteration scheme. The AC form of the governing equations are discretized using a second-order-accurate finite-volume method on the non-staggered computational grid. The convective terms are discretized using the second-order accurate, upwind-biased QUICK scheme, and central differencing is employed for the pressure gradients, viscous fluxes and source terms in the turbulence equation. The third-order, fourth-difference artificial dissipation method of Sotiropoulos and Abdallah (1991) is employed for pressure to eliminate odd–even decoupling of the pressure field. The physical time derivatives are discretized with three-point-backward, Euler-implicit temporal-integration scheme. The discrete equations are marched in time to advance the solution to the next time step by adopting the dual- (or pseudo-) time-stepping method. The system of equations is integrated in pseudo time using the pressure-based implicit preconditioner (Paik et al., 2005) enhanced with local-time-stepping and V-cycle multigrid acceleration. The computational domain is discretized using the domain decomposition approach with structured, overset (chimera) grids. We apply a set of characteristics-based, non-reflecting boundary conditions at the outlet of the computational domain to allow complex vortical structures to exit the computational domain without distortion. The numerical method has been extensively evaluated for calculating various turbulent shear flows in complex geometrical configurations (Paik et al., 2005, 2007; Paik and Sotiropoulos, 2005). For a detailed description of the numerical method the reader is referred to Paik et al. (2005). The code has been parallelized with MPI and run on a high performance computing cluster in the University of Minnesota Supercomputing Institute (MSI).

2.4. Computational details

We simulate flows past two cubes of height H mounted in tandem along the streamwise direction in a thin boundary layer ($\delta/H \approx 0.07$ where δ is the boundary layer thickness). Martinuzzi and Havel (2000) conducted an extensive experimental investigation of such flows for a broad range of cube spacings S_H and *Re* based on H and the bulk velocity. They observed that the measured flow patterns at *Re* = 22,000 are representative of the overall flow features for Reynolds numbers in the range 12,000–40,000. Among all their experimental configurations, therefore, we focus on two geometrical configurations with $S_H = 2$ and 4, respectively, at *Re* = 22,000. For both cases detailed experimental measurements have been published along with in-depth discussion of the flow physics (Martinuzzi and Havel, 2000, 2004).

For both $S_H = 2$ and 4, the upstream cube is located at a distance of $2H$ from the leading edge of the plate and the outlet boundary is placed at $x = 10H$ downstream of the leading edge of the first cube where the non-reflecting boundary conditions are applied (Paik et al., 2005). The lateral boundaries are placed symmetrically with respect to the streamwise plane of symmetry at $z = \pm 3.25H$ while the top boundary is placed at $y = 3.5H$. Zero gradient boundary conditions are used at all these boundaries. No-slip boundary conditions are applied on the bottom wall and the cube surface. Martinuzzi and Havel (2000) reported in their experiments that the inlet profile was uniform within 1% of the free stream velocity and the free stream turbulence intensity was less than 1.5%. To investigate the sensitivity of the numerical simulations to inflow disturbances, we carried out simulations using both steady and unsteady inflow conditions. The later were prescribed using a synthetic turbulence generation technique (Batten et al., 2004; Keating et al., 2006) by assuming homogeneous turbulent fluctuations of 1% turbulence intensity. Both steady and unsteady inflow

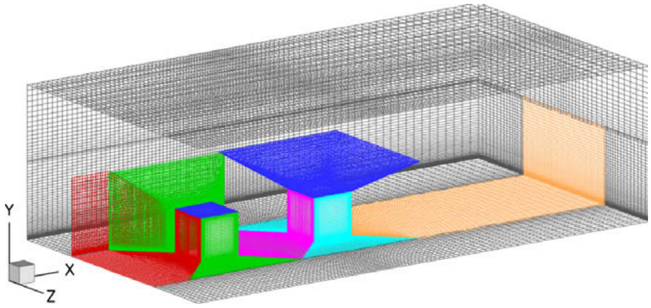

Fig. 1. Overset grids and the coordinate system.

conditions yielded essentially identical results for all cases and for all turbulence models. The results reported in the following section, however, have been obtained using the unsteady inflow conditions.

Fig. 1 shows the computational overset grids and the coordinate system for $S_H = 2$. The computational domain is discretized using domain decomposition with overset grids consisting of a total of 12 subdomains. The use of overset grids ensures fine resolution in the regions of interest without unnecessarily burdening the rest of the domain with the high aspect ratio cells that would result if the entire computational domain were to be discretized with a single set of coordinates. To explore the sensitivity of computed solutions to grid refinement for both cases, numerical simulations are carried out on two grids refined by a factor of 3/2 in all three directions: the coarse grid (cg) with approximately 0.82 million nodes; and the fine grid (fg) with 2.1 million nodes. For both the $S_H = 2$ and 4 cases, the number of grid nodes around the upstream cube is approximately twice as large as that around the downstream cube while overall grid resolutions in the inter-cube gap and the downstream cube wake are independent on the cube spacing. The first grid node off all solid walls is located at $y^+ \leqslant 1.0$ everywhere. The coarse and fine grid computations for both cases are carried out using nondimensional physical time steps of 0.025 and 0.02, respectively. Statistically converged URANS and DES results are obtained for nondimensional time of 400 and 800, respectively.

3. Results and discussion

For the $S_H = 2$ we carry out DES, DDES, DES-LR and URANS simulations while for reasons that will be apparent later in this section we only report DES-LR and URANS results for the second case. In what follows, we first present and discuss the computed time-averaged results and compare with the measurements of Martinuzzi and Havel (2000, 2004) in terms of mean flow quantities and oil-film visualizations. This is followed by the presentation of two- and three-dimensional visualizations of computed instantaneous flow fields to elucidate unsteady features of coherent vortical structures for the two different geometrical configurations and highlight the discrepancies between URANS and DES solutions. Finally we present and discuss the computed turbulence statistics along with the comparison with the measurements (Martinuzzi and Havel, 2000).

Time-averaged velocity vector fields computed at the streamwise plane of symmetry ($z = 0$) and at a horizontal plane ($y = 0.375$) for $S_H = 2$ are compared with the measurements (Martinuzzi and Havel, 2000, 2004) in Figs. 2 and 3, respectively. The measurements reveal two dominant large mean recirculation regions in the inter-cube gap and in the downstream cube wake at the plane of symmetry. The postfixes *-cg* and *-fg* in the turbulence model names, like DES-cg and DES-fg, stand for the coarse and fine grid computations, respectively. In these figures the computed velocity vectors are colored by the modeled eddy viscosity to indirectly show the relative importance of the LES mode and the low-Re correction of DES. Fig. 2 clearly shows that, unlike all DES models, URANS models most of the turbulent energy and yields flow fields which are insensitive to grid refinement. DES-cg, DDES-cg and DES-LR-cg appear to reproduce similar velocity fields and essentially identical eddy viscosity distributions, which are one order of magnitude smaller than that computed by URANS. Though some discrepancies are discernible in terms of vortex core location and overall shape, all computations except DES-fg and DDES-fg appear to reproduce with good accuracy the two main recirculating flow regions. In the inter-cube region URANS simulates a core location of the recirculating flow slightly lower and skewed upstream than the measurements while, in best agreement with the measurements, DES-LR-fg yields a slightly higher core without significant streamwise distortion. DES-fg and DDES-fg underestimate the intense reverse flow near the bottom plate in the inter-cube region.

The mean flow measured at the horizontal plane for $S_H = 2$ is characterized by the formation of two pairs of counter-rotating recirculation vortices in the inter-cube gap and the downstream cube wake, as shown in the measurements in Fig. 3. The measurements (Martinuzzi and Havel, 2000) further show that the development of the shear layer along the side faces of the downstream cube is strongly influenced by the flow impinging on its front face. As a result, large-scale oscillations of the wake flow lock-in with those of the gap flow (Martinuzzi and Havel, 2000). In terms of mean velocity vectors and the modeled eddy viscosity, the grid sensitivity of all numerical solutions at the horizontal plane is consistent with that at the vertical plane of symmetry shown in Fig. 2. Mean flow fields computed by URANS and all DES models do not show significant differences in the wake of the downstream cube, which agrees well with the measurements (Martinuzzi and Havel, 2000). Some differences between the various numerical solutions are found in the inter-cube region and near the side faces of the upstream cube. In the inter-cube region, URANS-cg and URANS-fg yield counter-rotating recirculating vortices which are slightly slimmer in shape than the measured ones and impinge on the side face of the downstream cube rather than on its front side edges. DES-LR-fg underestimates the velocity magnitude near the front side edges of the downstream cube but its solution is in better agreement with the measurements than URANS and other DES solutions in terms of overall shape of the counter-rotating vortices.

In both Figs. 2 and 3, a notable discrepancy is observed in the magnitudes of the eddy viscosity modeled by URANS and all DES models. URANS yields an eddy viscosity that is one order of magnitude higher than that computed by all DES models on the coarse mesh in the regions of interest. This discrepancy is responsible for URANS simulating only low-frequency large-scale spanwise oscillations in the inter-cube gap and in the wake of the downstream cube without resolving the smaller scales which are captured by DES-LR (see Figs. 11–13). DES-fg and DDES-fg yield fundamentally identical solutions with the subgrid eddy viscosity essentially negligible in most regions of interest. Along the vertical plane of symmetry, DES-fg and DDES-fg appear to reproduce the main recirculation regions similar in shape to those obtained from DES-LR-fg. However, both underestimate the intense reverse flow near the bottom surface in the inter-cube gap and fail to capture the rapid recovery of streamwise velocity profiles downstream of the second cube (roughly $x > 8$), as shown in Fig. 2. Furthermore, significant deterioration of DES-fg and DDES-fg solutions is observed on the horizontal plane. As show in Fig. 3 the solutions obtained with DES-fg and DDES-fg suffer from the emergence of spurious vortices that do not exist either in the measurements or in the URANS-fg and DES-LR-fg predictions. These vortices form at the upper and lower upstream edges of the second cube and

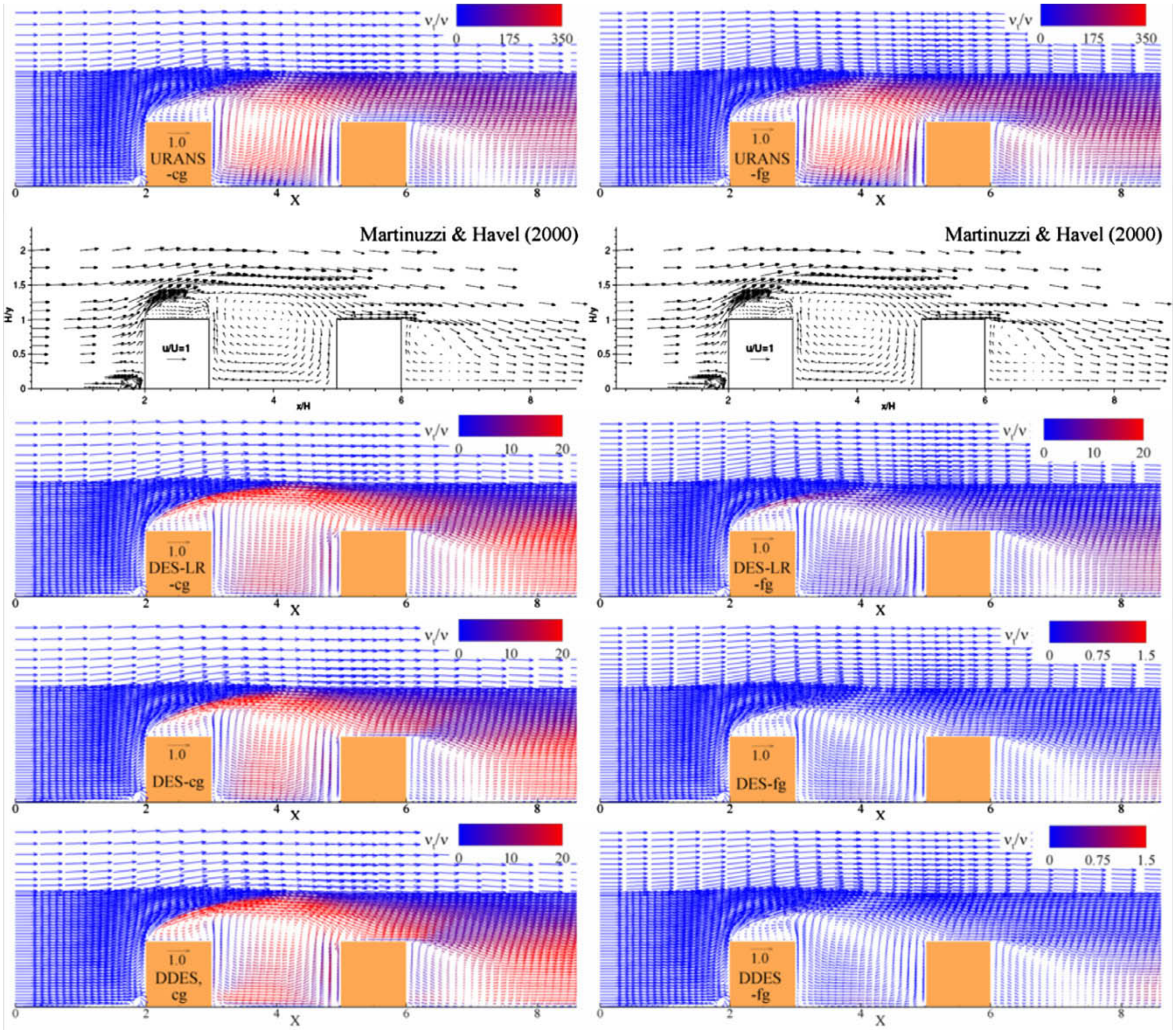

Fig. 2. Mean velocity vectors measured (Martinuzzi and Havel, 2000) and computed on the (*left*) coarse and (*right*) fine meshes at the vertical plane of symmetry $z = 0.0$ for the cube spacing $S_H = 2$. Computed vectors are plotted on the reconstructed mesh for visualization and colored by the modeled eddy viscosity.

should be attributed to the mis-interpretation of grid refinement as *wall proximity* in the inter-cube region. Note that the domain decomposition method with overset grids employed in this study allows us to efficiently impose high resolution in the inter-cube region. As pointed out by Spalart et al. (2006) and also observed in our computations, the mis-interpretation of grid refinement as *wall proximity* excessively lowers the subgrid eddy viscosity, relative to the ambient velocity and length scales, which results in a premature switch to unresolved DNS in the region where the local cell-Re is small. The resulting fast nonlinear drop of the subgrid eddy viscosity in the inter-cube region is thus responsible for the onset of the spurious vortex pair in the DES-fg and DDES-fg solutions. Our results clearly demonstrate that the low-*Re* correction of Spalart et al. (2006) employed in DES-LR successfully corrects this shortcoming of the standard DES model and eliminates the spurious vortices from the solution. Our results further suggest that the length scale modification of Spalart et al. (2006) employed in DDES-fg as the remedy for the so-called modeled-stress depletion accompanying spurious laminar-like premature separation apparently does not have a significant effect in our simulations. As shown in Figs. 2 and 3, on each grid, DES and DDES solutions are essentially identical in most regions of interest. This is consistent with results from a comparative study by Krishnan et al. (2006b) who reported that the DES and DDES predictions are essentially the same in the statistics as well as flow visualizations in simulations of flow around a circular cylinder at high *Re*. Note that in both cases of Krishnan et al. (2006b) and our study the flow domains contain regions of massive separation, wakes and thin boundary layers. Consequently, it is not surprising that the modification for delaying the LES mode in DDES does not work and that, as a result, DES and DDES yield the same results in these cases.

As shown in Fig. 4, which plots the measured (Martinuzzi and Havel, 2000) and computed mean velocity vectors at the plane of symmetry ($z = 0$) for $S_H = 2$, the mean flow in the upstream region of the first cube is dominated by the horseshoe vortex system. Although it is not clear in the measurements due to the coarse resolution near the bottom plate, Martinuzzi and Havel (2000) observed that the mean horseshoe vortex system actually consists of a complex structure involving a primary horseshoe vortex and at least two additional counter-rotating vortices upstream of the primary vortex in the thin laminar boundary ($\delta/H \approx 0.07$). Interestingly, all DES models and URANS yield essentially the same

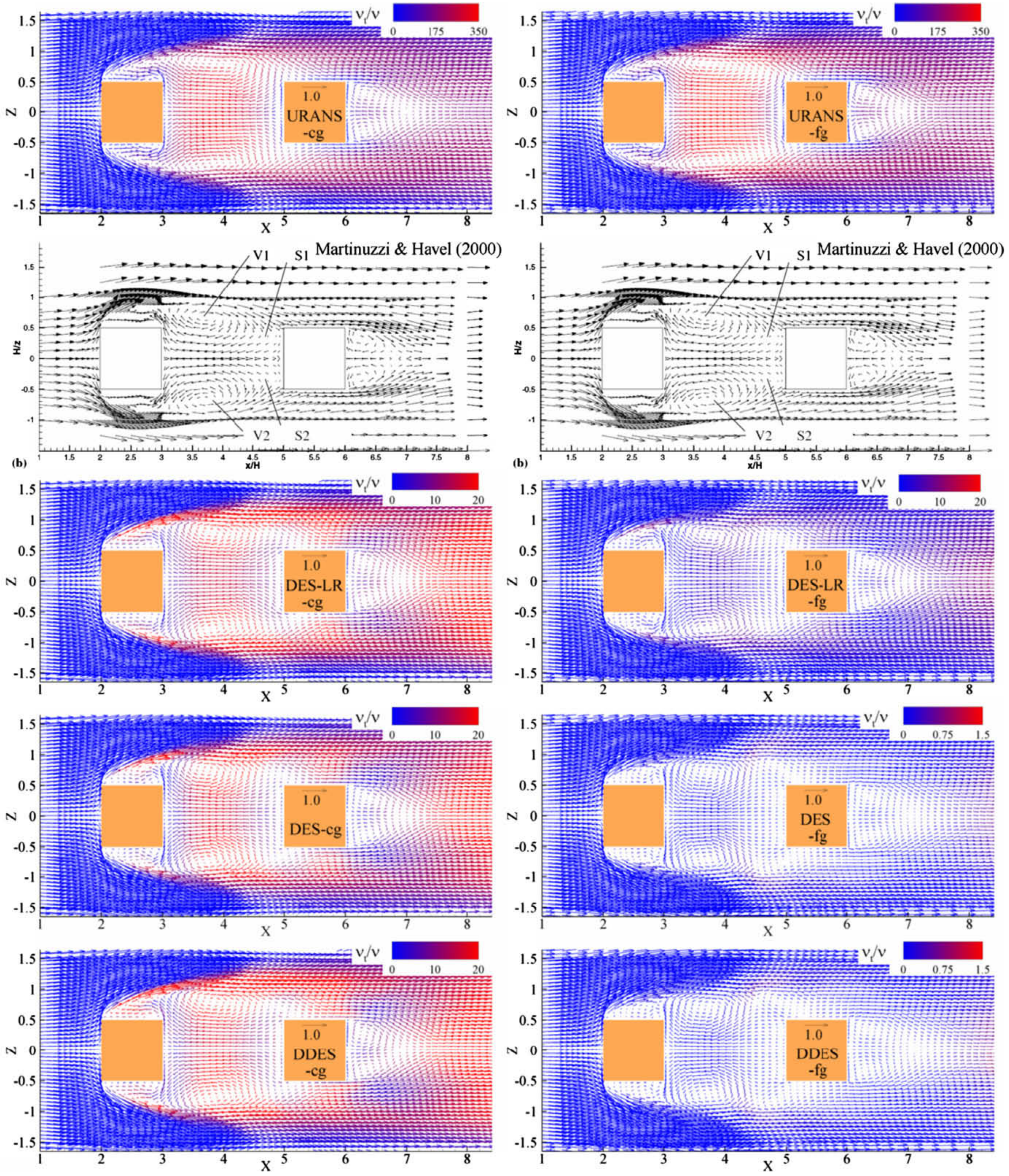

Fig. 3. Mean velocity vectors measured (Martinuzzi and Havel, 2004) and computed on the (*left*) coarse and (*right*) fine meshes at a horizontal plane ($y = 0.375$) for $S_H = 2$, as Fig. 2.

flow in the leading edge region and capture reasonably well the overall features of the horseshoe vortex system. A discrepancy between the measurements and the numerical predictions is that the computed primary mean horseshoe vortex is somewhat smaller in size and its core is located closer to the leading edge of the obstacle compared with the measurements (Martinuzzi and Havel, 2000). Specifically, the computed horseshoe vortex core is located approximately at $x = 1.83$ and $y = 0.09$ as compared to roughly $x = 1.78$ and $y = 0.11$ in the measurements, as shown in Fig. 4.

Interestingly, the trend that the predicted vortex is located closer to the obstacle than measured is exactly opposite to the

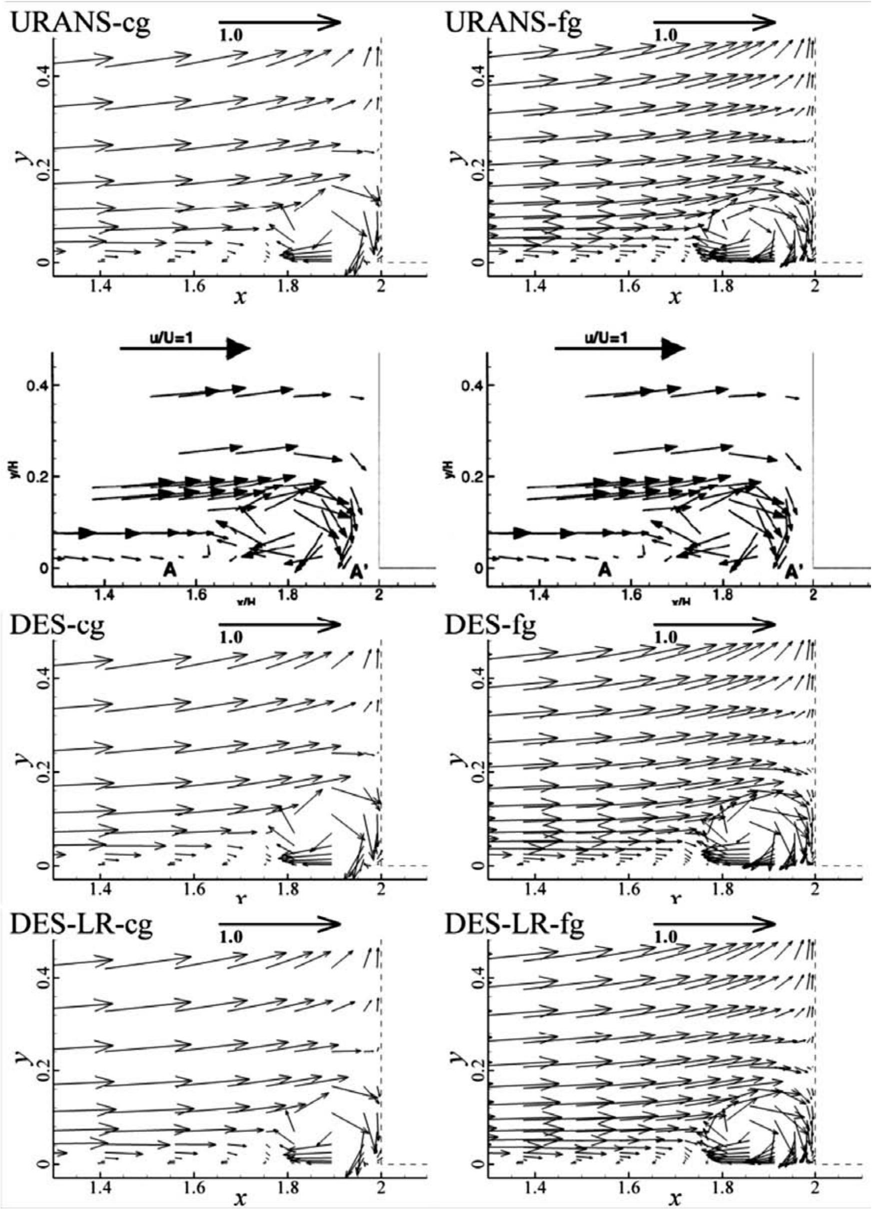

Fig. 4. Measured (Martinuzzi and Havel, 2000) and computed mean velocity vectors at the plane of symmetry $z = 0$ in the leading edge region of the upstream cube for $S_H = 2$. Computed vectors are plotted on every 4th horizontal and every 2nd vertical nodes.

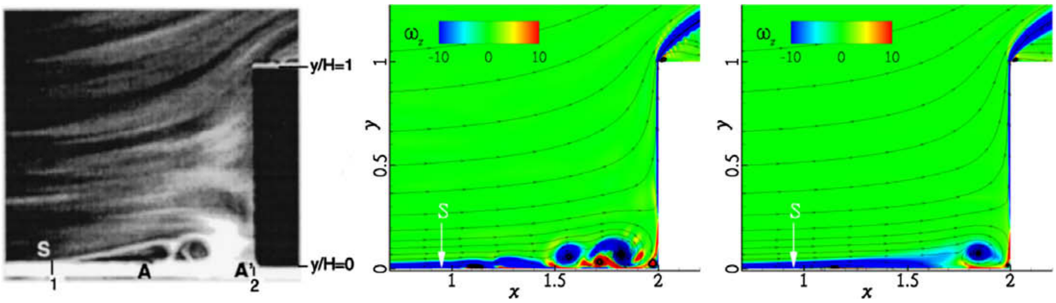

Fig. 5. Smoke visualization (Martinuzzi and Havel, 2000) and DES-LR-fg solution visualized by an instantaneous (*center*) and time-averaged (*right*) out-of-plane vorticity and streamlines at the plane of symmetry in the leading edge of the upstream cube for $S_H = 2$. Note that URANS-fg, DES-fg and DDES-fg solutions are essentially identical to DES-LR-fg solution in this region.

findings reported in recent numerical simulations (Paik et al., 2007) of the turbulent horseshoe vortex developing in the junction of a wing with a flat plate at much higher Reynolds number ($Re = 115{,}000$) and for a very thick incoming boundary layer ($\delta_{99}/T \approx 0.5$ where T is the wing maximum thickness) which was experimentally investigated by Devenport and Simpson (1990).

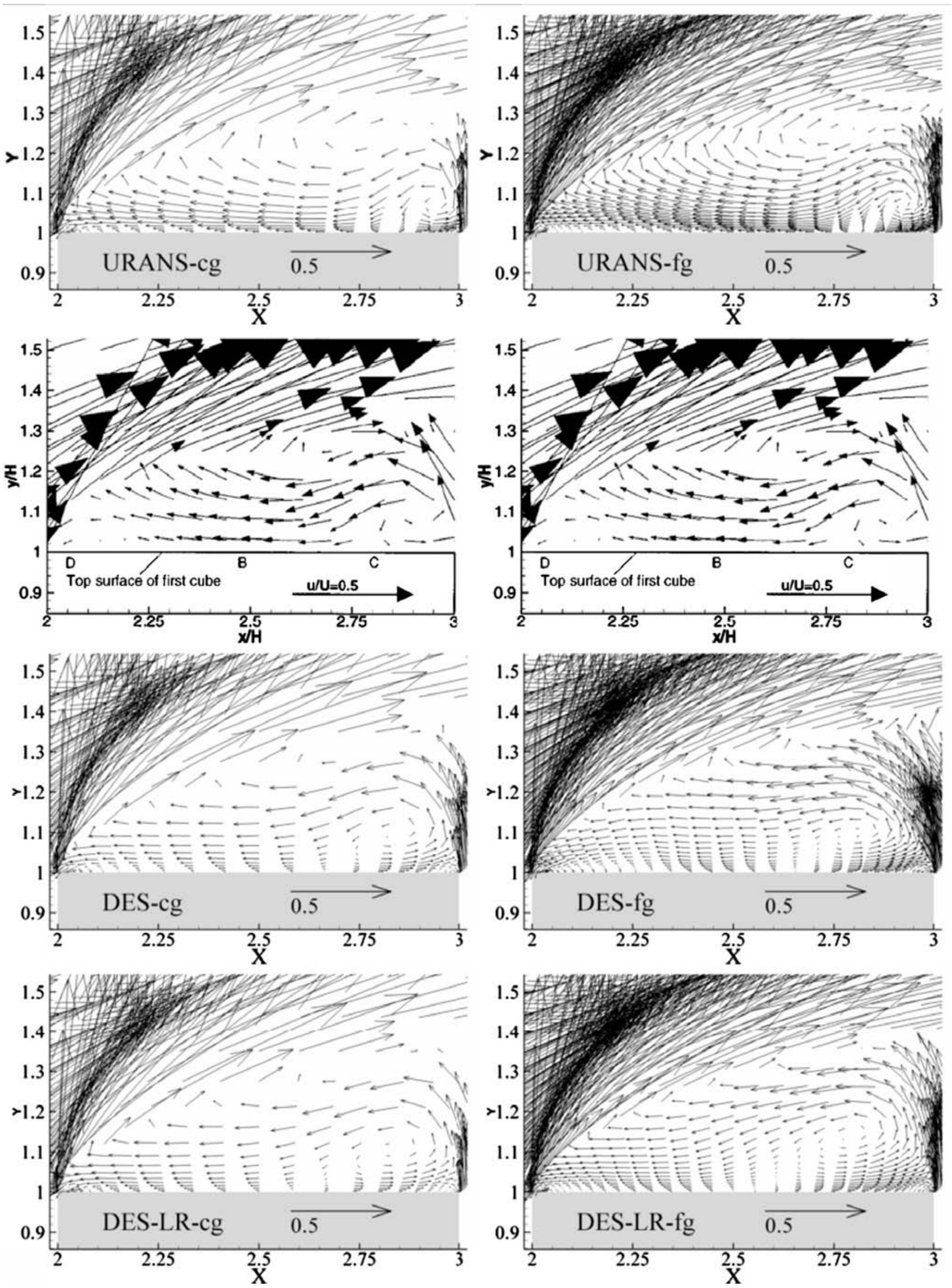

Fig. 6. Measured (Martinuzzi and Havel, 2000) and computed mean velocity vectors at the plane of symmetry $z = 0$ over the top face of the upstream cube for $S_H = 2$. Computed vectors are plotted on every 2nd horizontal and vertical nodes.

Paik et al. (2007) employed URANS and DES based on the S–A model to simulate the experiment of Devenport and Simpson (1990) and reported that the simulated vortex core is in fact located further upstream from the wing leading edge than measured. This excessive sensitivity of the S–A model to the adverse pressure gradient is also confirmed by Pasinato et al. (2004) who carried out the S–A model based RANS computation of the turbulent horseshoe vortex developing in the vane-endwall junction for the thick incoming boundary layer ($\delta_{99}/R \approx 0.62$ where R is the vane leading edge radius). The differences in the URANS and DES predictions of the vortex location should be due to the combined effect of the significant differences in the Reynolds number and the thickness of the approach boundary layer between the present case and that of the Devenport and Simpson experiment. Note that Paik et al. (2007) reported that for the Devenport and Simpson case URANS with the S–A model yields a steady horseshoe vortex system while the standard DES fails to resolve correctly the dynamics of the horseshoe vortex due to the aforementioned grid-induced modeled-stress depletion shortcoming. For this case the approach boundary is so thick that the entire horseshoe vortex system is embedded in the boundary layer and the condition for a well-posed DES (i.e. the requirement that the streamwise grid spacing should be greater than half the thickness of the boundary layer) is violated in the junction of the wing with the flat plate (see Paik et al., 2007 for details). Paik et al. (2007) had to device a flow-specific correction to the DES length scale that enforced a URANS layer in the near-wall region regardless of the local grid spacing. Such correction is not required in the present case because the approach

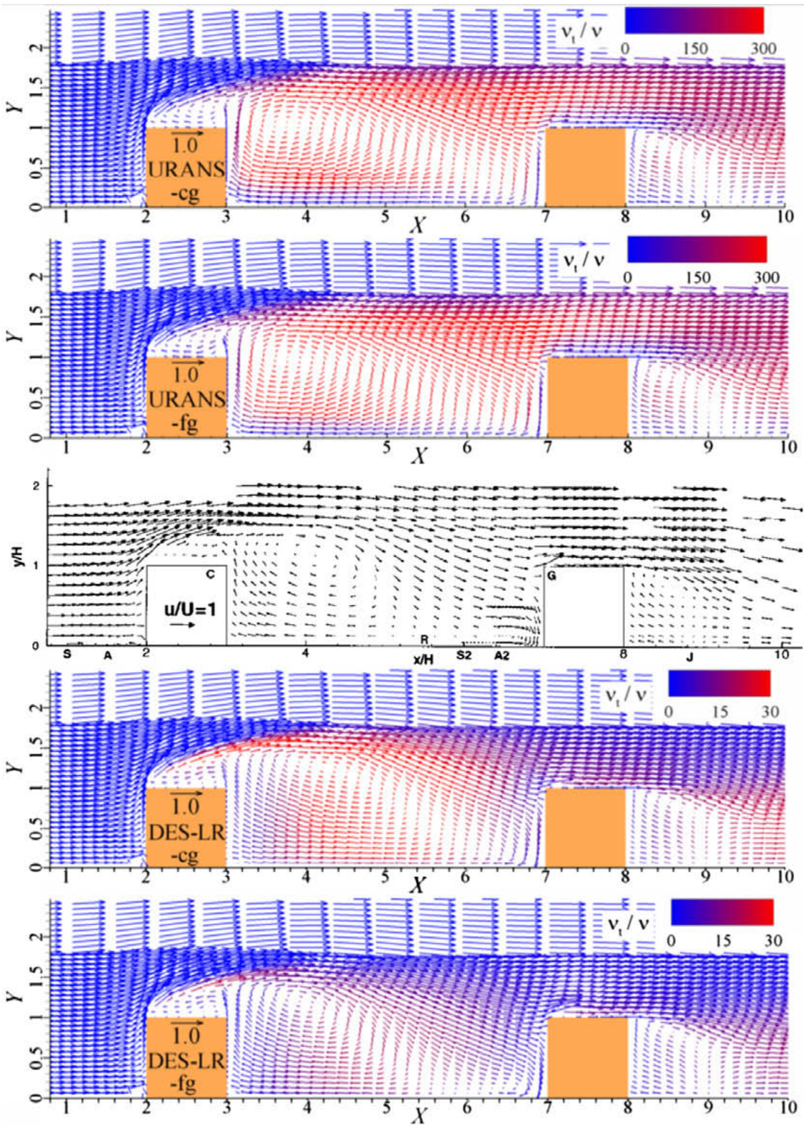

Fig. 7. Measured (Martinuzzi and Havel, 2000) and computed mean velocity vectors colored by the modeled eddy viscosity at the plane of symmetry $z = 0$ for the cube spacing S_H) = 4. Computed vectors are plotted on the reconstructed mesh for visualization.

boundary layer is sufficiently thin so that it is possible to construct a grid that ensures adequate resolution of the horseshoe vortex while satisfying the condition for a well-posed DES in the junction region. Furthermore, it is important to note that for all turbulence models employed herein, including the URANS model, the modeled eddy viscosity is negligible in the front face of the first cube. This should be attributed to the relatively low-Reynolds number of the present case which combined with the thin approach boundary layer and the very weak turbulence at the inlet plane results in an essentially laminar or at best transitional three-dimensional separation and vortex formation (see discussion of Fig. 5 below). This is a major difference between the present case and that of the Devenport and Simpson experiment and explains why for the former case both the URANS and all DES models resolve the unsteadiness of the vortex and yield essentially identical results in the junction region of the first cube while for the latter case URANS and standard DES failed to capture the coherent unsteadiness of the flow and the correct unsteady dynamics, respectively.

We also investigated the possible role of inflow disturbances on improving the prediction of the mean horseshoe vortex location. As shown in Shah and Ferziger (1997) and Krajnović and Davidson (2002) using turbulent inflow conditions for a thick incoming boundary layer case can significantly affect the predicted location of the vortex core. As we have already mentioned before, however, using steady or pseudo-turbulent inflow conditions in our case yielded for all turbulence models results identical to those shown in Fig. 4.

Martinuzzi and Havel (2000) carried out smoke visualization experiments to elucidate the unsteady features of the horseshoe vortex in the transitioning boundary layer upstream of the first cube. Their results are shown in Fig. 5 which shows that the incoming flow separates from the saddle point of separation roughly at $x = 0.95$ and that the horseshoe vortex system is dominated by multiple vortices upstream of the primary junction vortex close to the leading edge. The findings of Martinuzzi and Havel (2000) are entirely consistent with other horseshoe vortex experiments with thin and laminar incoming boundary layer Seal et al., 1995. The calculated instantaneous streamlines and out-of-plane vorticity contours snapshot also shown in Fig. 5 reveal that the computations capture the experimental trends. Furthermore, the corresponding time-averaged out-of-plane vorticity contours and streamlines also shown in the figure depict the existence of a mean

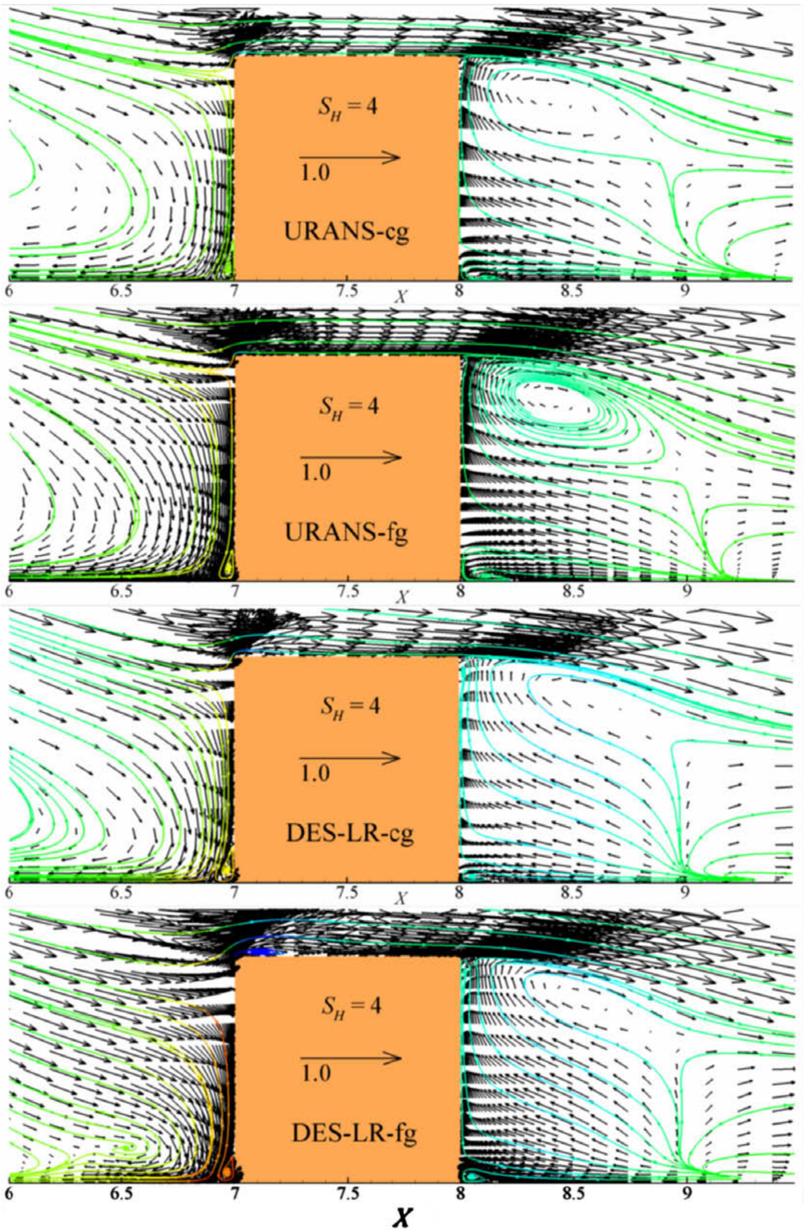

Fig. 8. Detailed view of time-averaged velocity vectors overlaid by mean streamlines colored by the mean pressure (blue, low; red, high) at the plane of symmetry $z = 0$ around the downstream cube for $S_H = 4$. Computed vectors are plotted on every second nodes. (For interpretation of the references to colour in this figure legend, the reader is referred to the web version of this article.)

horseshoe vortex (HSV) of negative vorticity and a thin layer of positive vorticity between the mean HSV and the bottom wall. The overall shape of the positive vorticity layer is comparable to those in previous studies for both laminar and turbulent boundary layers (Seal et al., 1995; Yakhot et al., 2006; Paik et al., 2007). Since detailed measurements in the leading edge region are not available and an in-depth investigation of the flow physics of the horseshoe vortex system in the thin laminar boundary layer is beyond the scope of this study, we will not elaborate further on this issue but pursue it in future work.

Fig. 6 shows the flow over the top surface of the upstream cube where the shear layer separates at the upstream leading edge and forms a distinct recirculation zone dominated by multiple vortices. This figure reveals that all numerical solutions are not sensitive to the grid refinement in this region. We leave out the vector plot of the DDES solutions on both grids in this figure because those are essentially identical to the DES solutions. The measurements of Martinuzzi and Havel (2000) show that the interplay among the shear layer, the top surface of the cube, the backflow from the inter-cube region, and its re-separation over the trailing edge of the top surface results in the formation of three main vortices whose core locations are visible at approximately $x = 2.15$, 2.7 and 2.9, respectively. In this region, URANS yields mean flow in better agreement with the measurements than all three DES. Although the backflow from the inter-cube region is relatively well reproduced in terms of its direction and velocity magnitude compared to the URANS solution, DES and DES-LR appear to overestimate the counter-rotating vortex induced by the re-separation of the backflow. This results in the underestimation of the reverse flow along the top face of the cube, as shown in Fig. 6.

When the cube spacing S_H is increased from 2 to 4, there is no significant change in the measurements around the upstream cube while the flow in the inter-cube and around the downstream cube appears to be, as one would reasonably anticipate, significantly

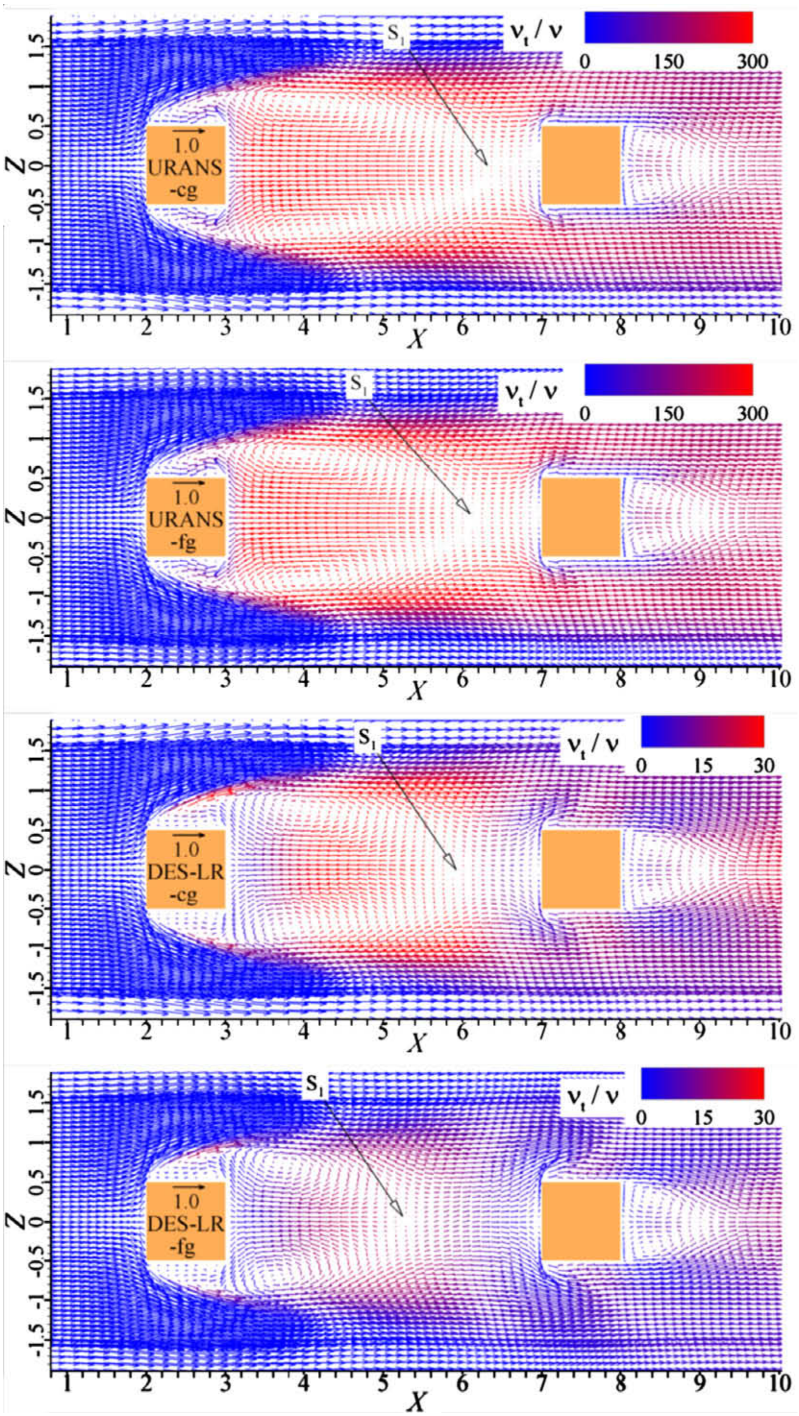

Fig. 9. Computed time-averaged velocity vectors colored by the modeled eddy viscosity at the vertical plane of symmetry ($y = 0.375$) for $S_H = 4$, as Fig. 7. No measurements (Martinuzzi and Havel, 2000) available.

dependent on the cube spacing. It is clearly visible in the measurements shown in Fig. 7 that for $S_H = 4$ the shear layer separating at the top leading edge of the upstream cube impinges on the front face of the second cube. The impingement of oncoming fluid results in a strong adverse pressure gradient, which leads to the formation of the second horseshoe vortex (SHV) system at the junction of the front face of the second cube and the bottom plate. Also, there is a region of upward moving fluid above the saddle point of attachment on the front face which re-separates at the front upper edge of the second cube and forms a short recirculation zone. As shown in Fig. 8, only DES-LR-fg captures these distinct vortical structures observed in the experiment for $S_H = 4$ around the downstream cube with good accuracy. In URANS-cg and URANS-fg, the stagnation point on the front face of the second cube is located closer to the top edge so that the re-separation does not occur near the top leading edge of the second cube. As a result, the computed adverse pressure gradient in front of the second cube appears to be too week to form SHV. The core of the primary recirculating flow computed by URANS is shifted upstream with respect to the measurements. Furthermore, URANS fails to capture the backflow from the inter-cube region to the top region of the upstream cube as well as the overall shape of the recirculation

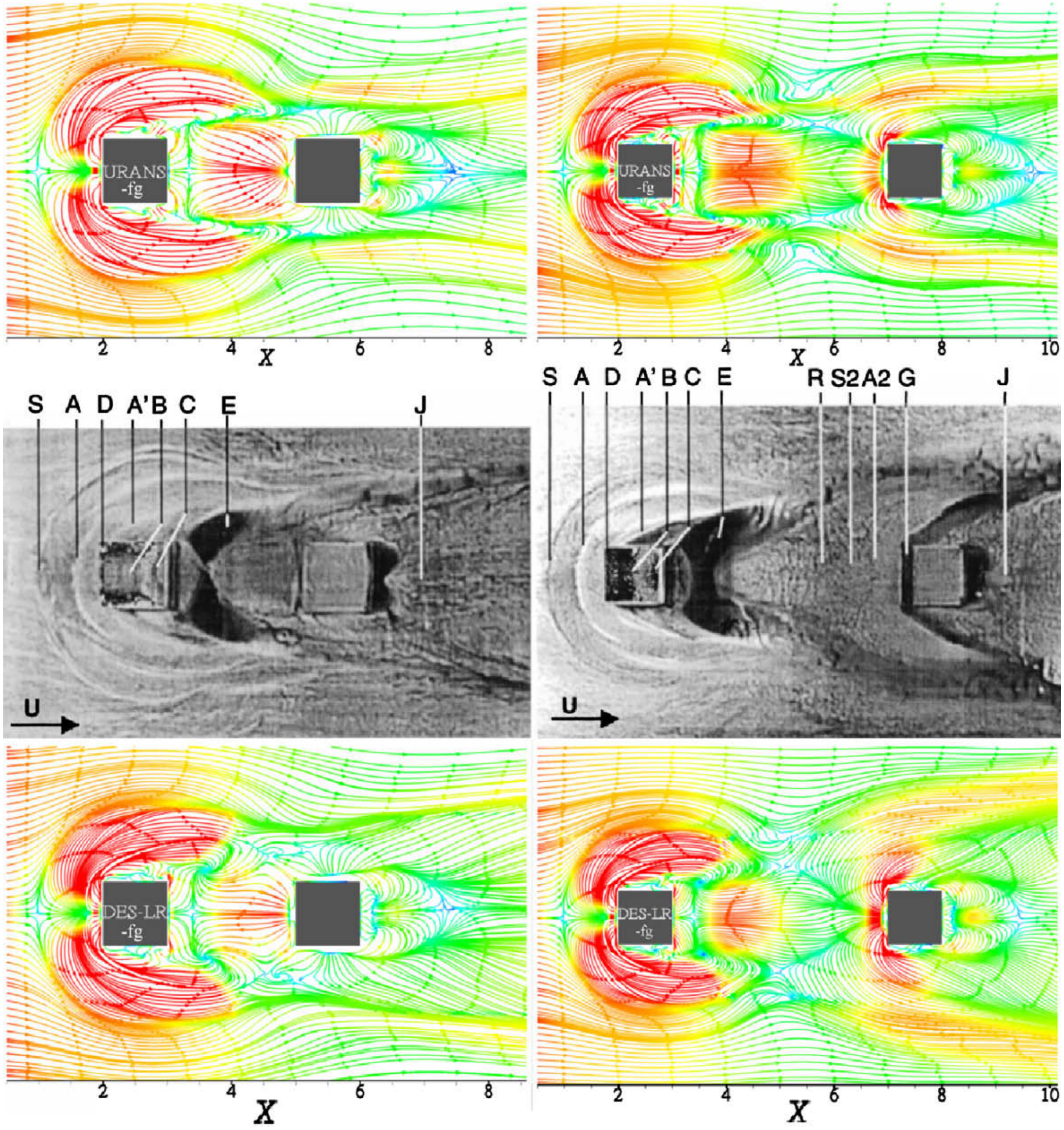

Fig. 10. Surface oil-flow visualization (Martinuzzi and Havel, 2000) and computed time-averaged friction lines colored by time-averaged shear velocity (blue, $u_\tau = 0.0$ and red, $u_\tau = 0.06$) for $S_H = 2$ and 4. (For interpretation of the references to colour in this figure legend, the reader is referred to the web version of this article.)

zone, as shown in Fig. 7. Interestingly, DES-LR-cg fails to capture the SHV. Though the core location of the primary recirculating flow is slightly higher than the measurement (Martinuzzi and Havel, 2000), DES-LR-fg appears to reproduce all measured mean flow features at the plane of symmetry with good accuracy. These results confirm that both an appropriately refined grid and the low-Reynolds number modification against the premature switch of the standard DES to unresolved DNS in low cell-*Re* regions are essential in DES for capturing detailed flow features around the two cubes. The computed mean recirculating flow downstream of the second cube does not appear to be significantly dependent on the cube spacing at the plane of symmetry, which is consistent with a series of experimental measurements of Martinuzzi and Havel (2000).

Due to the lack of measurements (Martinuzzi and Havel, 2000, 2004) for $S_H = 4$ at the horizontal plane, only the computed velocity vectors are plotted in Fig. 9. The primary counter-rotating vortices in the inter-cube region computed by URANS and DES-LR on both grids for $S_H = 4$ are consistent with those for $S_H = 2$. Both URANS-cg and URANS-fg solutions yield recirculation zones which are slimmer and longer in the streamwise direction than those obtained with the corresponding DES-LR solutions. A notable feature in the computed flow fields for $S_H = 4$ is that the pair of the saddle points S1 and S2 captured for $S_H = 2$ merge to form a single saddle point along the plane of symmetry. As shown in Fig. 9, DES-LR-fg yields a single saddle point roughly at $x = 5.3$ and $z = 0$ at the horizontal plane ($y = 0.375$) and strong streamwise flow impinging on the front surface of the downstream cube. These results are consistent with the measurements (Martinuzzi and Havel, 2000) shown in Fig. 7 as well as in the oil-film visualizations (see the subsequent paragraph and Fig. 10 for details). It is supported in this figure that an appropriately refined grid resolution is prerequisite to reproduce detailed flow features at this case. The eddy viscosity modeled by DES-LR-cg and DES-LR-fg is one order of magnitude smaller than that from URANS-cg and URANS-fg, which suggests that the LES mode of DES–LR explicitly resolves most of the

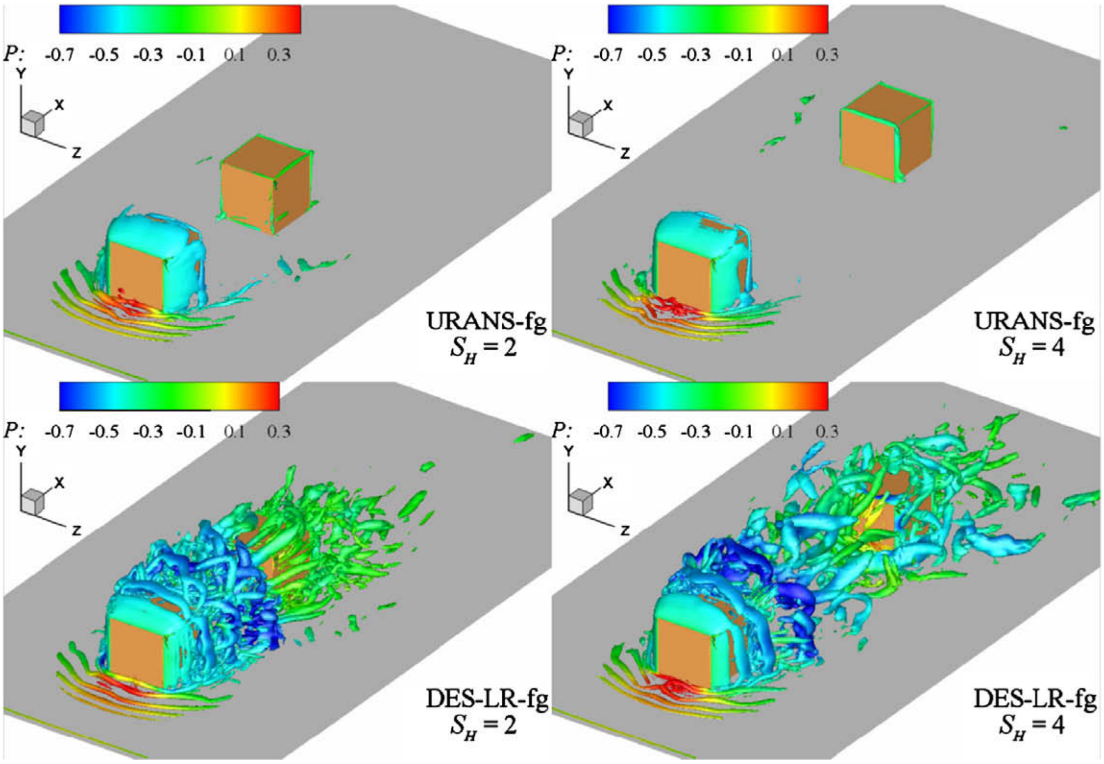

Fig. 11. Three-dimensional coherent structures around the two wall-mounted cubes identified by the instantaneous iso-surface of q-criterion ($q = 6$) colored by pressure computed for $S_H = 2$ and 4.

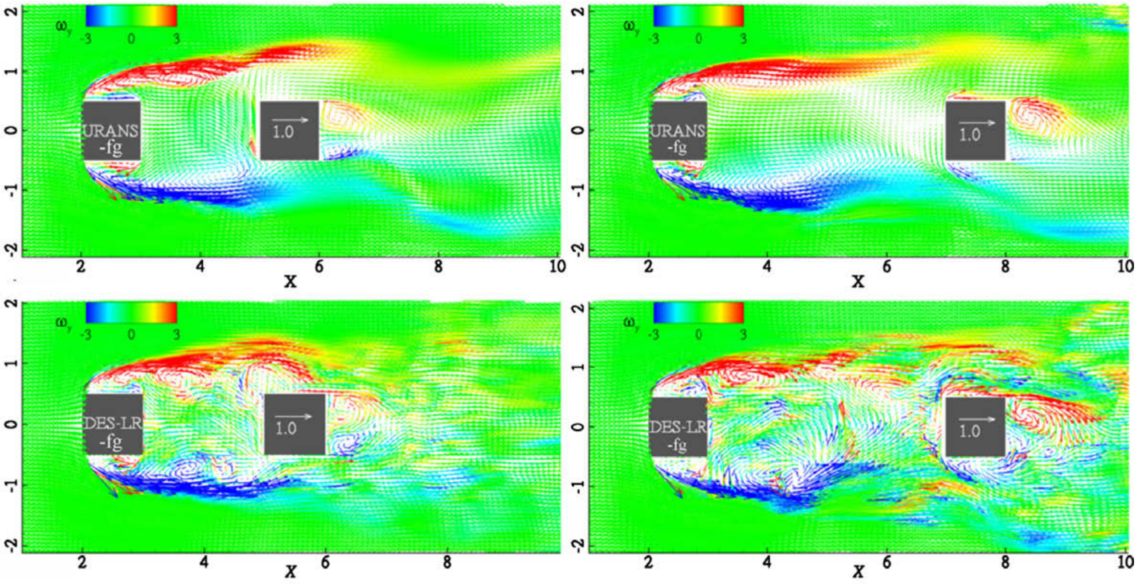

Fig. 12. Instantaneous velocity vectors colored by out-of-plane vorticity computed at the plane of symmetry $z = 0$ for $S_H = 2$ and 4. Vectors are plotted on the reconstructed mesh for visualization.

turbulence in the flow. As in the previous case, URANS computations appear to be insensitive to the grid refinement.

To study the topology of the surface shear stress patterns and characterize the regions of flow separation, reattachment and high surface shear on the plate, Martinuzzi and Havel (2000) applied an oil-film visualization technique. Their results are shown in Fig. 10 together with the calculated surface shear stress patterns identified by the time-averaged friction lines colored with the mean friction velocity u_τ (see Fig. 4 in Martinuzzi and Havel (2000) for details of the notation in the oil-film visualizations). In this figure and several subsequent figures associated with flow visualization, all coarse grid solutions are not included, because they are less meaningful than the fine grid solutions. We do not include also DES-fg and DDES-fg solutions which reveal somewhat more complicated vortical structures in the inter-cube region than DES-LR-fg, because DES-fg and DDES-fg suffer from the premature switch to unresolved DNS. The experimental visualization reveals the presence of two distinct lines wrapping around the upstream cube

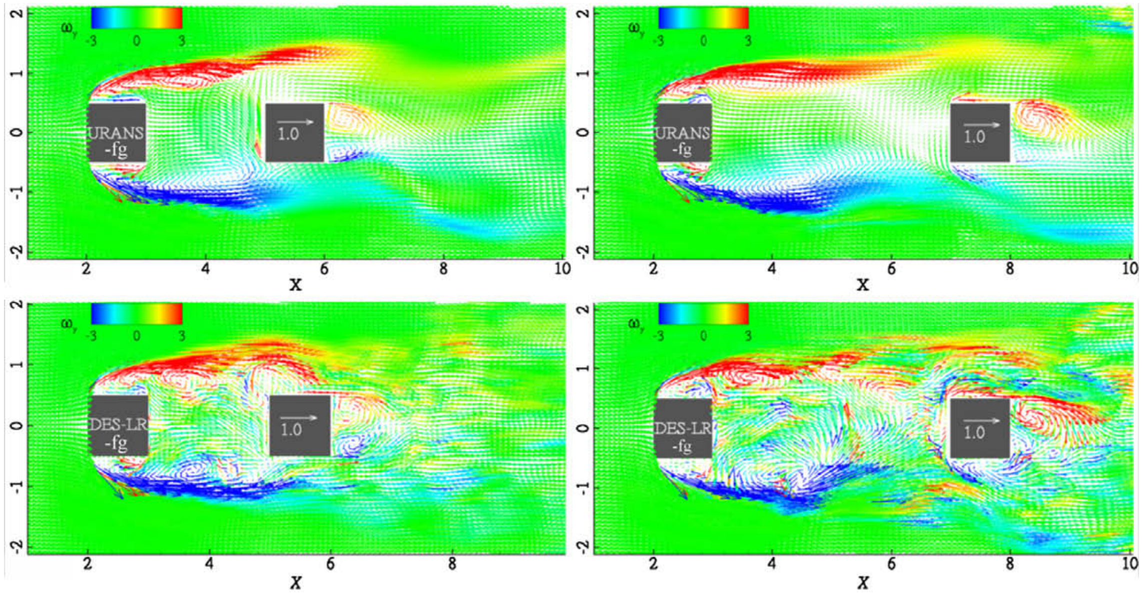

Fig. 13. Instantaneous velocity vectors colored by out-of-plane vorticity computed at a horizontal plane ($y = 0.375$) for $S_H = 2$ and 4, as Fig. 12.

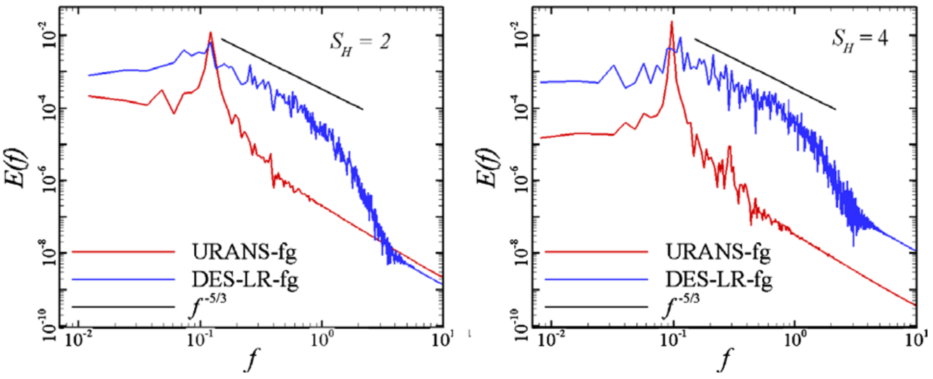

Fig. 14. Power spectra of velocity components resolved in the downstream wake for $S_H = 2$ and 4.

marked by S and A. The circulation due to the horseshoe vortex induces a high shear region on the plate, which results in a white band of low pigment accumulation marked with A directly upstream of the horseshoe vortex. This line remains close to the location of the horseshoe vortex as it wraps around the cube in necklace-like pattern (Martinuzzi and Havel, 2000). The pigment line S, which is farther upstream of the primary horseshoe vortex, originates at the saddle point at the plane of symmetry and marks the line where the approach boundary layer undergoes three-dimensional separation due to the adverse pressure gradient imposed by the upstream cube. The oil-film visualization also shows the footprints (dark pigment accumulation marked E) of a pair of counter-rotating vortices just downstream of the upstream cube for both $S_H = 2$ and 4 (Martinuzzi and Havel, 2000). Overall, these features of surface flow observed in the leading edge region of the upstream cube appear to be insensitive to S_H and are well reproduced by both URANS-fg and DES-LR-fg. In the inter-cube region and around the downstream cube, however, the measured near-wall flow patterns significantly depend on S_H, and URANS-fg and DES-LR-fg yield quite different solutions for each S_H. As shown in experimental visualizations of Martinuzzi and Havel (2000), the two lines S and A that wrap around the upstream cube merge into a single line at a distance of approximately $x = 4$ to form a distinct crescent-shaped region. The resulting single line bends inward toward the plane of symmetry until it reaches the location of roughly $x = 5$ where it is deflected away from the line of symmetry assuming an orientation that diverges slightly away form the line of symmetry. It is seen that the curvature associated with the footprint of the necklace-like horseshoe vortex is dependent on S/H. Upstream of the second cube, the experimental visualizations of Martinuzzi and Havel (2000) further show the lateral deflection of the resulting single line is much stronger for $S_H = 4$ than for $S_H = 2$. DES-LR-fg captures the curvature of the experimentally visualized near-wall patterns associated with the horseshoe vortices for both $S_H = 2$ and 4. URANS-fg fails to reproduce the significant streamwise variation of the surface flow patterns for both cases.

We now turn our attention to the evolution of coherent structures in the flow. To identify three-dimensional coherent structures in the simulated flow we employ the so-called q-criterion, based on the quantify $q = \frac{1}{2}(\|\Omega\|^2 - \|\mathbf{S}\|^2)$ where $\|\cdot\|$ is the Euclidean matrix norm and $\mathbf{S}$ and Ω denote the symmetric and antisymmetric parts of the velocity gradient (Hunt et al., 1988). Regions where $q > 0$ – i.e., where the rotation rate dominates the strain rate – are occupied by vortical structures. Although some deficiencies associated with local pressure minima and imposed non-uniform strain fields have been reported, the q-criterion has been found to identify coherent vortices with less sensitivity to numerical noise than the λ_2 method (Fraňa et al., 2005).

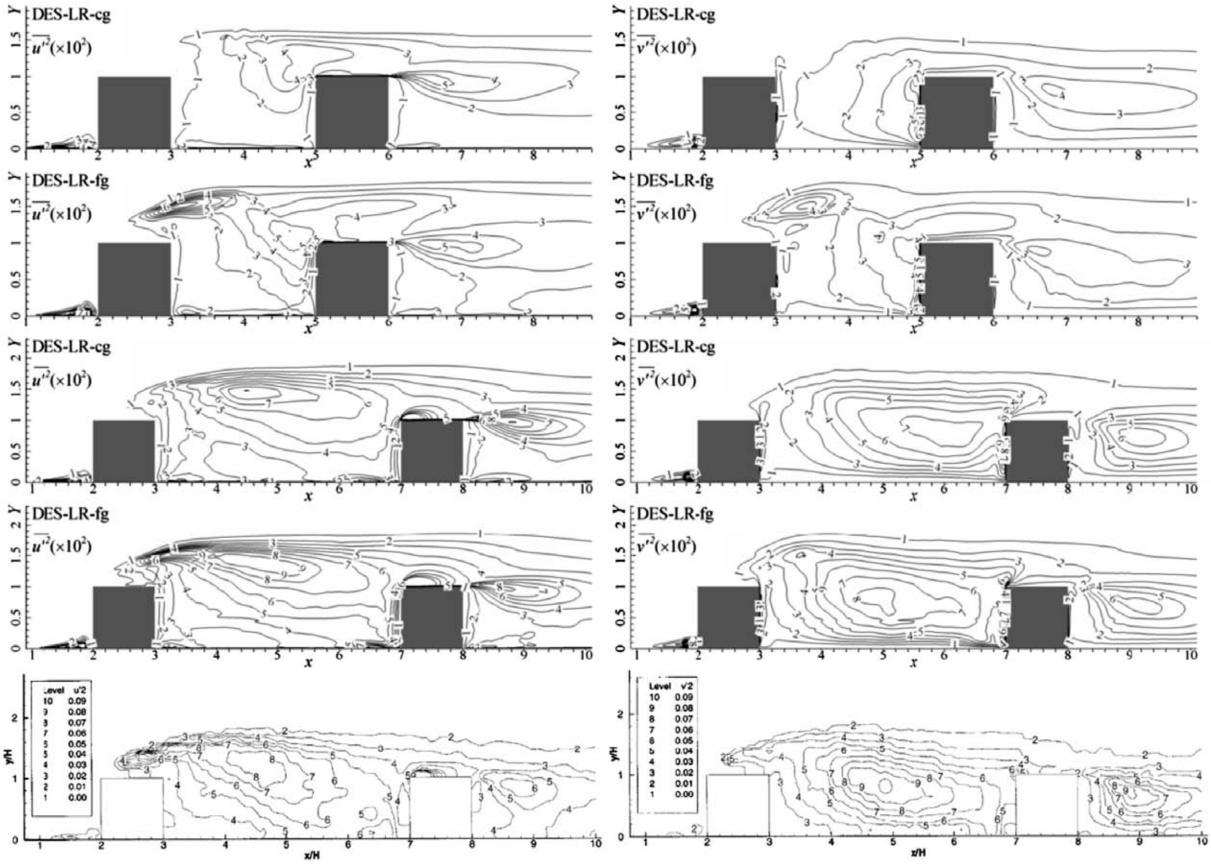

Fig. 15. Isolines of Reynolds normal stresses measured (Martinuzzi and Havel, 2000) and resolved by DES-LR-cg and DES-LR-fg at the plane of symmetry z=0 for $S_H = 2$ and 4. No measurements (Martinuzzi and Havel, 2000) are available for $S_H = 2$.

We apply the q-criterion to the instantaneous flow fields and construct video animations of the resulting coherent structures. Fig. 11 shows representative snapshots of q computed from URANS-fg and DES-LR-fg flow fields to elucidate overall features of the instantaneous flows for different cube spacings. The iso-surface of q criterion has been colored by the instantaneous pressure. This figure and our video animations show that the flows resolved by DES-LR-fg are dominated by very complex vortical structures that emerge in various regions. In the leading edge region of the upstream cube URANS-fg and DES-LR-fg yield essentially identical solutions, as shown in this figure, but their solutions are remarkably different in the downstream region. In the leading edge region of the upstream cube, the HSV system is characterized by the shedding of multiple vortices from the saddle point of separation located roughly at $x = 0.95$ and their merging into the primary HSV just upstream of the leading edge (see also Fig. 4). This horseshoe vortex system consisting of multiple vortices was also observed by Martinuzzi and Havel (2000) and also by Seal et al. (1995) in an earlier study of flow around a rectangular bluff body in a thin boundary layer.As shown in DES-LR-fg solutions, on the other hand, arch-type vortices are continuously shedding from the front edges of the upstream cube for both cases, which is consistent with the early experimental observations in flow around a single cube (Martinuzzi and Tropea, 1993). The DES-LR-fg solutions further show that arch vortices are twisted near their legs attached to the bottom plate as they move downstream due to the interaction with the solid wall. The interplay of arch vortices and the obstacle wake generates multiple hairpin and tube-like vortical structures in the inter-cube region. Some of these vortices are entrapped in the primary recirculation zones, and others move downstream and impinge on the surface of the downstream cube. The overall shape of these multiple vortices depends on the cube spacing, with longer vortices forming for larger grid spacings. Our video animations constructed by instantaneous snapshots further show that the wake structures, including these tube-like vortices, oscillate in the spanwise direction.

Instantaneous velocity vectors colored with the out-of-plane vorticity component at the plane of symmetry and at a horizontal plane ($y = 0.375$) are plotted in Figs. 12 and 13, respectively. It is evident from the comparison of the instantaneous snapshots shown in these figures and the mean flow fields shown in Figs. 2, 3, 7 and 9 that URANS-fg captures only large-scale horizontal oscillations of the wake structures in the inter-cube and the downstream wake regions, but fails to reproduce the rich dynamics of coherent vortical structures. Note that URANS-cg yields solution which is essentially identical to URANS-fg solutions. In contrast, this comparison clearly demonstrates that DES-LR-fg yields very rich instantaneous flow fields for the two cases studied by Martinuzzi and Havel (2000, 2004). More specifically, the DES-LR-fg solutions shown in Fig. 12 along with our video animations depict that for $S_H = 4$ the shear layer emanating leading edge of the upstream cube undergoes more intense fluctuations in the vertical direction in the inter-cube region than that for $S_H = 2$ and impinges on the front face of the second cube. The impingement of oncoming fluid results in a strong adverse pressure gradient which leads to the formation of a second horseshoe vortex system in the leading edge region of the downstream cube. It is also recognizable from the comparison of instantaneous flow fields shown in Fig. 13 and the time-averaged ones plotted in Figs. 3 and 9 that the primary vortices are periodically advected downstream in alternating fashion.

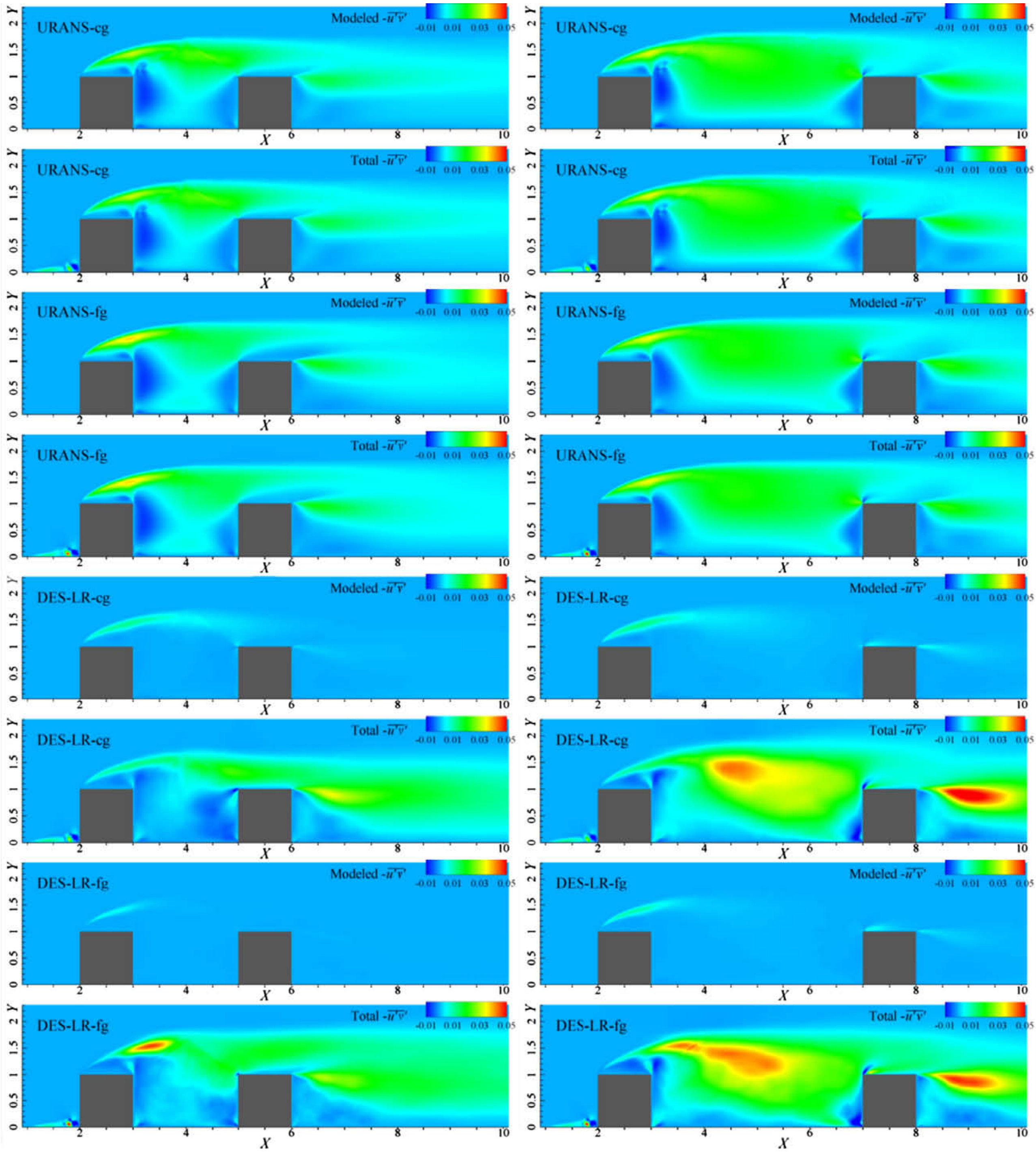

Fig. 16. Modeled and total (modeled + resolved) Reynolds shear stresses $-\overline{u'v'}$ at the plane of symmetry $z = 0$ for $S_H = 2$ and 4.

The shear layers emanating from the side edges of the upstream cube attach on the side surfaces of the downstream cube for $S_H = 2$, while they attach on the front surface of the downstream cube for $S_H = 4$. All these features of instantaneous flow fields computed by DES-LR-fg are consistent and in good qualitative agreement with the experimental observations of Martinuzzi and Havel (2000, 2004).

To identify the dominant vortex shedding frequency of the two-cube wake, power spectrum density functions of the streamwise velocity component resolved by URANS-fg and DES-LR-fg at a point 2H downstream of the rear face of the second cube at the plane of symmetry are plotted in Fig. 14. Martinuzzi and Havel (2000) observed that the frequency of the spectral peak in the downstream wake ranges from 0.095 for $S_H = 2$ to 0.105 for $S_H = 4$ asymptotically increasing with increasing S_H to reach a value of 0.11, which corresponds to the case of a single cube. As shown in Fig. 14, both URANS-fg and DES-LR-fg capture the dominant frequencies in good agreement with the measurements. However, URANS-fg reproduces only the large-scale wake structure at the lowest dominant frequency while DES-LR-fg yields several harmonics associated with the interaction of the wake downstream of the second cube and the shear layer originating from the side leading edge of the

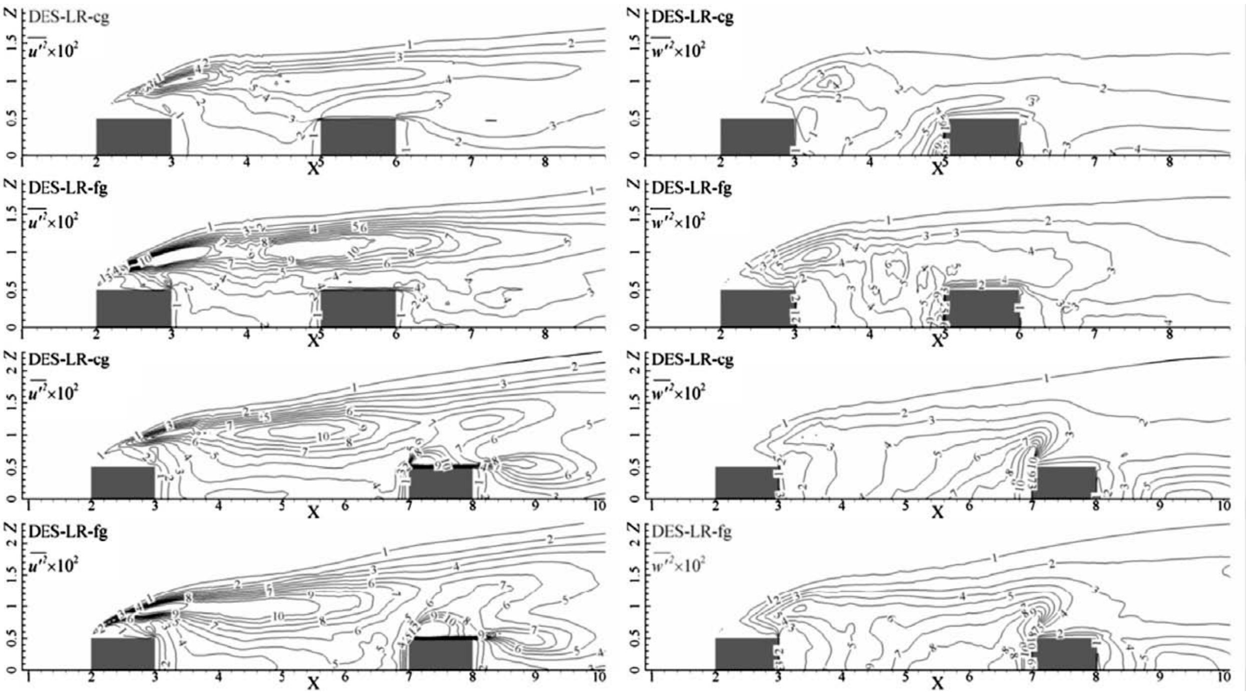

Fig. 17. Isolines of Reynolds normal stresses resolved by DES-LR at a horizontal plane $y = 0.375$ for $S_H = 2$ and 4.

upstream cube as well as the dominant wake frequency. Furthermore, DES-LR-fg results in velocity spectra that exhibit a clear $-5/3$ power law inertial subrange for both $S_H = 2$ and 4.

The measured and resolved Reynolds normal stresses $\overline{u'^2}$ and $\overline{v'^2}$ at the plane of symmetry are compared in Fig. 15. Note that only the resolved part of the Reynolds stresses calculated by DES-LR on the coarse and fine grids are plotted in this figure. The components modeled by DES-LR are negligible in most regions of interest except in the shear layer just above the top surface of the upstream cube. URANS solutions are not included in this figure because the resolved components obtained with URANS are negligible except in the region of the horseshoe vortex upstream of the first cube. Although it is impossible to validate the Reynolds normal stresses computed for $S_H = 2$ due to the lack of the measurements (Martinuzzi and Havel, 2000), we include the results in Fig. 15 to compare with those computed for $S_H = 4$. In the measurements of Martinuzzi and Havel (2000), the horseshoe vortex regions are discernible as pockets of high $\overline{u'^2}$ and $\overline{v'^2}$ in the leading edge of the upstream cube for both $S_H = 2$ and 4. In particular, in the $S_H = 4$ case, high turbulence level pockets mark the location of the second horseshoe vortex upstream of the second cube (Martinuzzi and Havel, 2000). These features of measured turbulent statistics are qualitatively and quantitatively well resolved by DES-LR-fg in most regions of interest. Only in the upstream part of the shear layer emanating from the top leading edge of the upstream cube the level of the resolved components are lower than the measurements, which can be explained by the fact that Reynolds stresses in that region are not fully resolved and their modeled components are significant (see Fig. 16 for further details). For $S_H = 4$, DES-LR-cg appears to yield Reynolds stress distributions where the intensity of both $\overline{u'^2}$ and $\overline{v'^2}$ are underestimated than in DES-LR-fg solutions and their peak locations are distorted comparing to the measurements (Martinuzzi and Havel, 2000) in the inter-cube gap. The Reynolds normal stresses predicted by DES-LR-fg for $S_H = 2$ appear to be lower than the corresponding solutions for $S_H = 4$ in the inter-cube region and the downstream cube wake. Their values over the top and in the leading edge region of the upstream cube do not appear to be sensitive to the cube spacing. These results are consistent with the measurements of Martinuzzi and Havel (2000) who observed that the length of the inter-obstacle spacing has negligible influence on the turbulence levels in the region upstream and above the first cube in the separation zone.

To further explore the capability of URANS and DES-LR to reproduce turbulence statistics in the flows under consideration, we compare in Fig. 16 the modeled and total (modeled plus resolved) Reynolds stress $-\overline{u'v'}$ at the plane of symmetry. Note that, unfortunately, measurements of Reynolds shear stresses are not available. This figure confirms that Reynolds stresses in the leading edge region of the upstream cube are fully resolved by all simulations regardless of the turbulence models. However, several remarkable discrepancies between URANS and DES-LR solutions are discernible in these figures. As mentioned earlier in this paper and also observed by Martinuzzi and Havel (2000), the turbulence level in the inter-cube region increases for $S_H = 4$. In the inter-cube gap, the main recirculation region at the plane of symmetry exhibits elevated levels of turbulence stresses as the inter-obstacle spacing is increased. It is evident in Fig. 16 for instance that, as the cube spacing is increased, the computed Reynolds stresses are significantly enhanced in both the inter-cube and the downstream wake regions. The comparison of Figs. 15 and 16 further confirms that DES-LR-fg resolves most of Reynolds stresses with good agreement with the measurements (Martinuzzi and Havel, 2000) while URANS significantly underestimates the Reynolds stresses, particularly for the larger cube spacing, and most of stresses are modeled.

The Reynolds normal stresses resolved by DES-LR-fg at a horizontal plane ($y = 0.375$) are plotted in Fig. 17. As in Fig. 15, URANS-fg solutions are not included in this figure due to the negligible level of the resolved components. As mentioned previously, URANS fails to resolve the aforementioned flapping motion and the interaction with the downstream cube of the shear layer emanating from the top leading edge of the upstream cube while resolves only a part of Reynolds stresses associated with the large-scale, low-frequency wake structures downstream of both cubes near the bottom flat. That is, URANS reproduces only a periodic spanwise oscillations of the wake structures with a dominant frequency and without harmonics reproduced by DES-LR as also

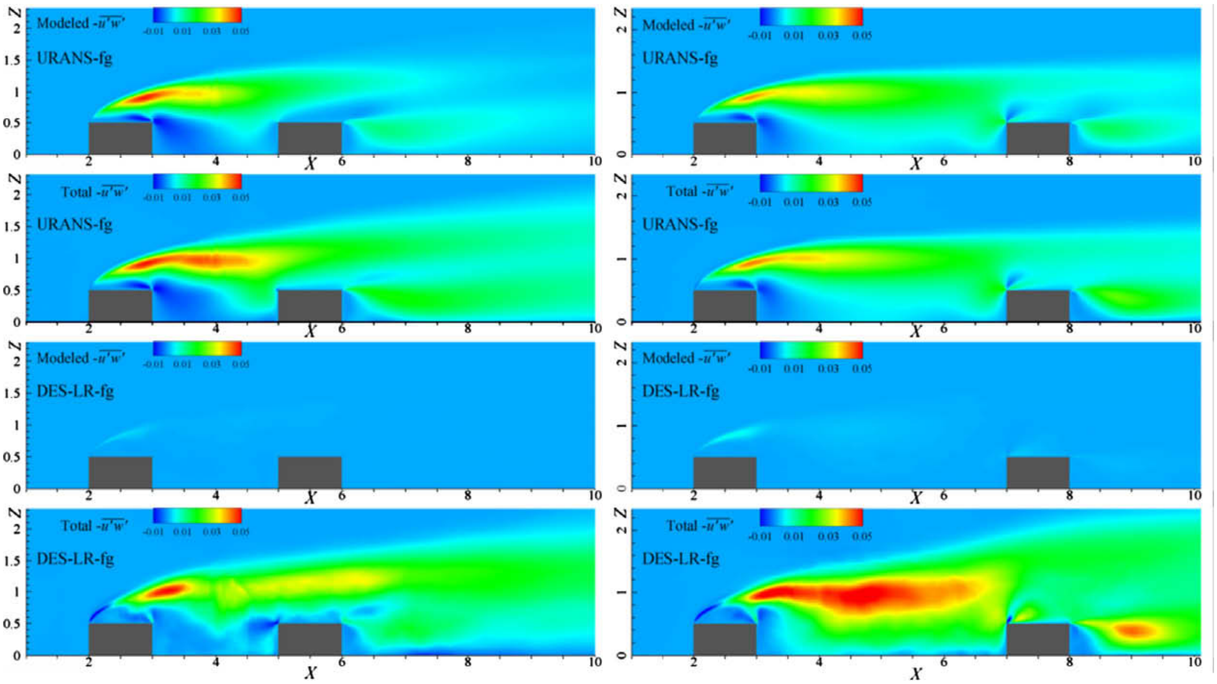

Fig. 18. Modeled and total (modeled + resolved) Reynolds shear stresses $-\overline{u'w'}$ at a horizontal plane $y = 0.375$ for $S_H = 2$ and 4.

shown in Fig. 14. This result from the URANS computations is further supported by Fig. 18, which shows the modeled and total Reynolds shear stress $-\overline{u'w'}$. In the URANS computations, as shown in Fig. 18, most of the Reynolds stresses are modeled at the horizontal plane as at the plane of symmetry shown in Fig 16. Fig. 18 shows that the high shear stress region computed by DES-LR-fg at the horizontal plane is inflected outward past the downstream cube for $S_H = 4$. This feature is attributed to the development of the second horseshoe vortex in the leading edge region of the downstream cube and is consistent with the oil-flow visualizations of Martinuzzi and Havel (2000) and the friction lines computed by DES-LR-fg. In terms of the turbulent intensity, furthermore, DES-LR-fg yields increased level of Reynolds stresses as the cube spacing increases, which is also consistent with the computed and measured results previously shown in Figs. 15 and 16.

4. Conclusions

We investigated the performance of URANS with the S–A model, the standard DES proposed by Spalart et al. (1997) and its two recently proposed modifications, DDES and DES-LR (Spalart et al., 2006), by applying them to simulate the flow around two wall-mounted cubes in tandem with two different cube spacings, $S_H = 2$ and 4, at a moderate *Re* of 22,000. The sensitivity of each model to grid refinement was studied via computations on two successively refined grids. Several important conclusions are drawn from this study based on the comparison of numerical solutions with the measurements of Martinuzzi and Havel (2000, 2004).

The predictive capabilities of the various turbulence models are found to vary significantly in various regions of the flow. All turbulence models yield essentially identical results in the upstream junction region between the first cube with the flat wall. The simulations resolve a dynamically rich horseshoe vortex system consisting of several vortices that are shed continuously from the upstream point of separation. The good agreement between all turbulence models in this region should be attributed to the combined effect of the very thin approach boundary layer, the low levels of turbulence intensities at the inlet and the relative low-Reynolds number of the flow, which result in an essentially laminar or at most transitional three-dimensional separation and vortex formation. The predicted time-averaged horseshoe vortex is in good overall agreement with the measurements but the mean location of the vortex is somewhat closer than measured to the first cube.

In the inter-cube and downstream regions of the flow significant discrepancies are observed among all four turbulence models. URANS underpredicts significantly the intense large-scale fluctuations of the flow and consequently grossly underpredicts the Reynolds stresses in this region and fails to capture even gross mean flow features, such as the overall curvature and general structure of the lines of separation wrapping around the two-cube system in the limiting streamlines along the bottom wall and the second horseshoe vortex that forms at the upstream junction of the second cube with the bottom wall for $S_H = 4$. It is worth noting, however, that URANS even though it only resolves very large-scales of motion does capture correctly the dominant shedding frequency in the wake of the second cube. Also URANS yields the best overall agreement between the computations and the measurements for the mean flow patterns in the separated flow region at the top of the first cube. The grid sensitivity study shows that URANS solutions are essentially insensitive to the grid refinement.

All DES models on the coarse grid (DES-cg, DDES-cg and DES-LR-cg) yield almost identical flow field, which is similar to the URANS solution. All DES models fail to capture some key features of the mean velocity field, such as the development of the second horseshoe vortex in the leading edge of the downstream cube. In contrast, DES solutions on the fine grid (DES-fg, DDES-fg, DES-LR-fg) reproduce different flow fields. Both the DES-fg and DDES-fg solutions exhibit the well-known shortcoming of DES in the inter-cube region of the flow. These two computations yield identical results in the inter-cube gap with a spurious vortex pair forming in the vicinity of the second cube. This non-physical behavior should be attributed to the premature switch of DES to under-resolved DNS in this region of the flow, which is characterized by low overall velocities and thus low local cell Reynolds numbers. The DES-LR model is shown to effectively remedy this shortcoming of DES as on the fine grid yields both mean flow and turbulence statistics that are in very good overall agreement with the measurements. Furthermore, DES-LR-fg is shown to directly resolve most scales of motion in the flow in the inter-cube and wake regions as evidenced by the computed spectra, which not only resolve correctly the dominant shedding frequency but also exhibit a well defined −5/3 power law inertial subrange. The only discrepancy between the measurements and the DES-LR approach is observed in the separated region above the first cube where, as we already mentioned, URANS yields the best overall prediction of the measured mean vortical patterns.

Overall our results confirm that the low-*Re* correction of Spalart et al. (2006) employed in DES-LR is a good remedy for the non-physical behavior of DES in low cell-*Re* regions of the flow. In most regions of interest, DES-LR-fg yields mean flow, turbulence statistics, and instantaneous flow patterns that are in good qualitative and quantitative agreement with the measurements.

Acknowledgements

This work was supported by NSF grants–EAR-0120914 (as part of the National Center for Earth-surface Dynamics) and EAR-0738726 and a grant (Code # '06 CTIP B-01) from the Construction Technology Innovation Program (CTIP) funded by from the Ministry of Land, Transport and Maritime Affairs of Korean government. This work was carried out in part using computing resources at the University of Minnesota Supercomputer Institute.

References

Batten, P., Goldberg, U., Chakravarthy, S., 2004. Interfacing statistical turbulence closures with large-eddy simulation. AIAA J. 42 (3), 485–492.

Castro, I.P., Robins, A.G., 1977. The flow around a surface-mounted cube in uniform and turbulent streams. J. Fluid Mech. 79, 307–335.

Devenport, W.J., Simpson, R.L., 1990. Time-dependent and time-averaged turbulence structure near the nose of a wing-body junction. J. Fluid Mech. 210, 23–55.

Fraňa, K., Stiller, J., Grundmann, R., 2005. Taylor–Görtler vortices in the flow driven by a rotating magnetic field in a cylindrical container. J. Visual. 8 (4), 323–330.

Hedges, L.S., Travin, A.K., Sparlart, P.R., 2002. Detached-eddy simulation over a simplified landing gear. ASME J. Fluid Eng. 124 (2), 413–423.

Hunt, J.C.R., Wray, A.A., Moin, P., 1988. Eddies, stream, and convergence zones in turbulent flows. In: Proceeding of the Summer Program. Center for Turbulence Research, NASA Ames/Stanford Univ., pp. 193–208.

Hussein, H., Martinuzzi, R.J., 1996. Energy balance for turbulent flow around a surface-mounted cube placed in a channel. Phys. Fluid 8 (3), 764–780.

Iaccarino, G., Ooi, A., Durbin, P.A., Behnia, M., 2003. Reynolds-averaged simulation of unsteady separated flow. Int. J. Heat Fluid Flow 24, 147–156.

Keating, A., Prisco, G.D., Piomelli, U., 2006. Interface conditions for hybrid rans/les calculations. Int. J. Heat Fluid Flow 27, 777–788.

Krajnović, S., Davidson, L., 2002. Large-eddy simulation of the flow around a bluff body. AIAA J. 40 (5), 927–936.

Krishnan, V., Squires, K.D., Forsythe, J.R., 2006a. Prediction of separated flow characteristics over a hump. AIAA J. 44, 252–262.

Krishnan, V., Squires, K.D., Forsythe, J.R., 2006b. Prediction of the flow around a circular cylinder at high reynolds number. AIAA Paper 2006-901.

Martinuzzi, R., Havel, B., 2000. Turbulent flow around two interfering surface-mounted cubic obstacles in tandem arrangement. ASME J. Fluid Eng. 122, 24–31.

Martinuzzi, R., Havel, B., 2004. Vortex shedding from two surface-mounted cubes in tandem. Int. J. Heat Fluid Flow 25, 364–372.

Martinuzzi, R., Tropea, C., 1993. The flow around surface-mounted, prismatic obstacles placed in a fully developed channel flow. ASME J. Fluid Eng. 115, 85–92.

Meinders, E.R., Hanjalić, K., 1999. Vortex structure and heat transfer in turbulent flow over a wall-mounted matrix of cubes. Int. J. Heat Fluid Flow 20, 255–267.

Meinders, E.R., Hanjalić, K., 2002. Experimental study of the convective heat transfer from in-line and staggered configurations of two wall-mounted cubes. Int. J. Heat Mass Transfer 45, 465–482.

Menter, F.R., Kuntz, M., Bender, R., 2003. A scale-adaptive simulation model for turbulent flow predictions. AIAA Paper 2003-0767.

Ničeno, B., Dronkers, A.D.T., Hanjalić, K., 2002. Turbulent heat transfer from a multi-layer wall-mounted cube matrix: a large-eddy simulation. Int. J. Heat Fluid Flow 23, 173–185.

Paik, J., Escauriaza, C., Sotiropoulos, F., 2007. On the bi-modal dynamics of the turbulent horseshoe vortex system in a wing-body junction. Phys. Fluid 19 (4), 045107.

Paik, J., Sotiropoulos, F., 2005. Coherent structure dynamics upstream of a long rectangular block at the side of a large aspect ratio channel. Phys. Fluid 17 (11), 115104.

Paik, J., Sotiropoulos, F., Sale, M.J., 2005. Numerical simulation of swirling flow in a hydroturbine draft tube using unsteady statistical turbulence models. ASCE J. Hydraul. Eng. 131 (6), 441–456.

Pasinato, H.D., Squires, K.D., Roy, R.P., 2004. Assessment of Reynolds-averaged turbulence models for prediction of the flow and heat transfer in an inlet vane-endwall passage. ASME J. Fluid Eng. 126, 305–315.

Rodi, W., 1997. Comparison of LES and RANS calculations of the flow around bluff bodies. J. Wind Eng. Ind. Aerodyn. 69, 55–75.

Rodi, W., Ferziger, J., Breuer, M., Pourquié, M., 1997. Status of large-eddy simulation: results of a workshop. ASME J. Fluid Eng. 119, 248–262.

Schmidt, S., Thiele, F., 2002. Comparison of numerical methods applied to the flow over wall-mounted cubes. Int. J. Heat Fluid Flow 23, 330–339.

Schofield, W., Logan, E., 1990. Turbulent shear flow over surface-mounted obstacles. ASME J. Fluid Eng. 112, 376–385.

Seal, C.V., Smith, C.R., Akin, O., Rockwell, D., 1995. Quantitative characteristics of a laminar necklace vortex system at a rectangular block-flat plate juncture. J. Fluid Mech. 286, 117–135.

Shah, K.B., Ferziger, J.H., 1997. A fluid mechanicians view of wind engineering: large-eddy simulation of flow past a cubic obstacle. J. Wind Eng. Ind. Aerodyn. 67, 211–224.

Sotiropoulos, F., Abdallah, S., 1991. The discrete continuity equation in primitive variable solutions of incompressible flow. J. Comput. Phys. 95, 212–227.

Spalart, P., Deck, S., Shur, M., Squires, K., Strelets, M., Travin, A., 2006. A new version of detached-eddy simulation, resistant to ambiguous grid densities. Theor. Comput. Fluid Dyn. 20 (3), 181–195.

Spalart, P.R., Allmaras, S.R., 1994. A one-equation turbulence model for aerodynamic flows. La Recherche Aerospatiale 1, 5–21.

Spalart, P.R., Jou, W.H., Strelets, M., Allmaras, S.R., 1997. Comments on the feasibility of LES for wings, and on a hybrid RANS/LES approach. In: Liu, C., Liu, Z. (Eds.), Advances in DNS/LES. Greyden Press, Columbus, OH.

Squires, K.D., Forsythe, J.R., Spalart, P.R., 2005. Detached-eddy simulation of the separated flow over a rounded-corner square. ASME J. Fluid Eng. 127 (3), 959–966.

Yakhot, A., Anor, T., Liu, H., Nikitin, N., 2006. Direct numerical simulation of turbulent flow around a wall-mounted cube: spatio-temporal evolution of large-scale vortices. J. Fluid Mech. 566, 1–9.